

# Characterizing the High Strain Rate Mechanical Behavior of Stainless Steel 316L Processed by Selective Laser Melting

by  
Travis J. Kneen

Submitted in Partial Fulfillment of the Requirements  
for the Degree of  
Master of Science  
in the  
Mechanical Engineering  
Program

YOUNGSTOWN STATE UNIVERSITY

May 2016

Characterizing the High Strain Rate Mechanical Behavior of Stainless Steel 316L Processed  
by Selective Laser Melting

Travis J. Kneen

I hereby release this thesis to the public. I understand that this thesis will be made available from the OhioLINK ETD Center and the Maag Library Circulation Desk for public access. I also authorize the University or other individuals to make copies of this thesis as needed for scholarly research.

Signature: \_\_\_\_\_  
*Travis J. Kneen, Student* Date

Approvals: \_\_\_\_\_  
*Dr. Brett Conner, Thesis Advisor* Date

\_\_\_\_\_  
*Dr. Jae Joong Ryu, Committee Member* Date

\_\_\_\_\_  
*Dr. Pedro Cortes, Committee Member* Date

\_\_\_\_\_  
*Dr. Virgil Solomon, Committee Member* Date

\_\_\_\_\_  
*Dr. Salvatore A. Sanders, Dean of Graduate Studies* Date

## Abstract

Additive manufacturing (AM), especially 3D printing, can produce more complex parts and decrease lead times when compared to traditional manufacturing processes. The 3D printing of stainless steel 316L is of particular interest for applications in vehicular crashworthiness, foreign object damage impact resistance, and armor for its combination of strength, toughness, and corrosion resistance. As additive manufacturing becomes more prevalent, components for these applications will be 3D printed. Creating highly dense finished parts with mechanical and material properties comparable to traditionally manufactured parts is an obstacle currently hampering the expansion of AM. In particular, defects and porosity resulting from certain 3D printing process parameters adversely affect the mechanical properties of a finished part. This can significantly hinder AM's ability to expand its use in the aforementioned industries. Therefore, it is important to characterize and understand how such defects affect finished parts with a combination of mechanical testing and microstructural analysis.

In order to achieve this, stainless steel 316L parts were printed on a Renishaw AM250 selective laser melting (SLM) machine using two different printer process parameter sets and various build orientations. Both dynamic and quasi-static strain rate mechanical tests were used to determine the mechanical properties, which were compared to wrought stainless steel 316L plate and other reported additive manufacturing results. Analysis was done to determine any microstructural changes or defects in the specimens. The first set of process parameters resulted in specimens that did not achieve properties comparable to wrought stainless steel. The second set of process parameters resulted in

specimens with greatly improved properties. Specimens of both sets exceeded the yield strengths of wrought plate. At high strain rates, the SLM specimens demonstrated strain-rate sensitivity with increased tensile and yield strengths compared to quasi-static results, but not as high as wrought plate. With further process optimization, acceptable SLM 316L parts should meet industrial expectations and be useful in high strain rate applications.

## Acknowledgements

I would like to first off thank my advisor, Dr. Brett Conner, for his assistance with this work. The path to completing this had some obstacles that made the process a bit unconventional and without his continued patience and understanding this would not have been possible. I would also like to thank my thesis committee consisting of Dr. Virgil Solomon, Dr. J.J. Ryu, and Dr. Pedro Cortes for revising this work and giving advice countless times when asked. For funding of numerous of the equipment and my research I want to acknowledge the Youngstown State University Research Council, the Army Research Laboratory (Split-Hopkinson Pressure Bar), the NSF support DMR #1229129 (field emission SEM), and Ohio Board of Regents Grant S932-12 (variable pressure SEM). I want to thank M-7 Technologies for assistance in machining parts off of the substrate and Bancroft Farms for machining the notches for the Charpy specimens. For the massive amounts of help in the numerous experiments I want to recognize Dr. Matt Zeller (XRF/XRD), Dr. Guha Manogharan, and several YSU students: Matt Caputo (SEM), Kyle Myers (SHPB), Shobha Subedi (impact and hardness tests), Chris Barrett (etching and microscopy), and Ashley Bowers (SLM printing and hardness tests).

For advising me to join YSU and, specifically, the graduate program I want to thank Dr. Hazel Marie and Dr. Mike Crescimanno. For sparking my interest in additive manufacturing I want to recognize America Makes (the National Additive Manufacturing Innovation Institute, NAMII) and especially Kevin Collier and Rodrigo Gutierrez for the countless hours of support with the Renishaw AM250 machine.

Last, but not least, I want to thank my friends and family who have stuck by me and kept me going through the entire adventure. Special thanks to my parents and my siblings for always believing in me and making sure I finished my work.

# Table of Contents

Abstract.....	iii
Acknowledgements.....	v
List of Figures.....	x
List of Tables.....	xiv
Chapter 1: Introduction.....	1
1.1 Additive Manufacturing.....	1
1.1.1 Selective Laser Melting.....	4
1.1.2 Process Parameters.....	6
1.1.3 Post-Processing.....	13
1.2 Microstructural Analysis.....	15
1.3 Mechanical Testing.....	19
1.3.1 Hardness Testing.....	20
1.3.2 Quasi-Static Tensile Testing.....	23
1.3.3 Split-Hopkinson Compression Testing.....	28
1.3.4 Charpy V-Notch Impact Testing.....	32
1.3.5 Fracture and Fatigue Testing.....	34
1.4 Research Objectives.....	37
Chapter 2: Materials and Methods.....	38

2.1 Materials .....	38
2.1.1 Powder Distribution Analysis .....	38
2.1.2 Powder Chemistry Analysis.....	40
2.2 Builds .....	40
2.3 Microstructural Analysis.....	44
2.3.1 Preparation of Samples .....	44
2.3.2 Polished Surface Analysis.....	45
2.3.3 Fracture Surface Analysis .....	46
2.4 Mechanical Testing.....	46
2.4.1 Hardness Testing.....	46
2.4.2 Quasi-Static Tensile Testing .....	47
2.4.3 Split-Hopkinson Compression Testing .....	50
2.4.4 Charpy V-Notch Impact Testing.....	52
Chapter 3: Results and Discussion.....	54
3.1 Powder Analysis .....	54
3.1.1 Powder Sizing and Distribution.....	54
3.1.2 Powder Chemistry.....	55
3.2 Microstructural Analysis.....	57
3.3 Mechanical Testing.....	63



3.3.1 Hardness Testing.....	63
3.3.2 Quasi-Static Tensile Testing.....	65
3.3.3 Split-Hopkinson Compression Testing.....	75
3.3.4 Charpy V-Notch Impact Testing.....	78
Chapter 4: Conclusions and Future Work.....	84
References.....	87
Appendix.....	98

## List of Figures

Figure 1: A typical SLM process schematic [6] .....	4
Figure 2: Schematics of scanning speed of the laser (a), exposure time of the laser (b), and point distance of the laser (c) [7].....	8
Figure 3: Six scan strategies tested by Kruth et al. [27] .....	10
Figure 4: Schematic of a single layer meandering scan strategy [10] .....	11
Figure 5: Islands scanning strategy [19] .....	12
Figure 6: SEM image of polished section with a balling induced pore by Li et al. [35]..	17
Figure 7: (a) Optical micrograph of grain boundaries in 316L etched with Vilella's reagent; (b) SEM image of the cellular structure at the intersection of two misaligned melt pools [12] .....	19
Figure 8: General characteristics of hardness testing methods [50] .....	21
Figure 9: Stress-strain curve demonstrating how to determine ultimate tensile and 0.2% yield strengths [51] .....	24
Figure 10: Stress strain curves of AM produced Ti-6Al-4V tensile specimens printed in three orientations [13].....	26
Figure 11: Split-Hopkinson pressure bar setup for a compression specimen, where it is important to note that the specimen diameter is smaller than the bar diameters [55] .....	29
Figure 12: Lee et al. results of quasi-static and SHPB compression testing of different density 316L samples at different strain rates [57].....	31

Figure 13: Fracture surfaces of SLM produced Ti-6Al-4V+10Mo Charpy V-notch specimens. The white arrows indicate crack growth direction with the insert showing build direction [21]. .....	33
Figure 14: Three modes of loading relative to a crack [64].....	35
Figure 15: Cilas 1190 laser particle size analyzer and the schematic of how it determines particle sizes [69] .....	39
Figure 16: Renishaw AM 250 Internal Diagram [33].....	41
Figure 17: Orientation of the three orthogonal specimen orientations labelled according to ASTM F2921 [13].....	44
Figure 18: ASTM E8/8M-09 rectangular tension test specimen schematic [51].....	48
Figure 19: Tensile test schematic [78] .....	50
Figure 20: Specimen setup between incident and transmission bars of SHPB [79].....	51
Figure 21: Typical wave response capture in SURE-Pulse from specimen 3 from the ZX-2 group. The point of the first simultaneous incident/transmitted wave signal is chosen for analysis.....	51
Figure 22: ASTM E370 standard dimensions for Charpy V-notch specimens [60].....	52
Figure 23: Notch orientations for each specimen group.....	52
Figure 24: Schematic of Charpy V-Notch mechanism [81] .....	53
Figure 25: Particle size distribution measured using Cilas 1190 in liquid mode.....	54
Figure 26: Secondary backscatter images of powder at 150x magnification (a), 500x magnification (b), and 1800x magnification (c) .....	55

Figure 27: (a) Parameter 1 <i>XY</i> orientation polished sample examined under 100x light microscope and (b) 150x secondary electron micrograph of the same sample. ....	58
Figure 28: (a) Parameter 1 <i>ZX</i> orientation polished sample examined under 100x optical and (b) 150x secondary electron micrograph of the same sample.....	59
Figure 29: (a) Parameter 2 <i>XY</i> orientation polished sample examined under 100x optical and (b) 150x secondary electron micrograph of the same sample.....	60
Figure 30: (a) Parameter 2 <i>ZX</i> orientation polished sample examined under 100x optical and (b) 50x secondary electron micrograph of the same sample.....	60
Figure 31: (a) 50x optical micrographs of parameter set 1 and (b) set 2 showcasing the SLM microstructure .....	61
Figure 32: Continuous cooling transformation (CCT) diagram of a low carbon steel showing the different structures possible at different cooling rates [83].....	62
Figure 33: Stress-strain curves of the first set of parameters and wrought plate components using strain gages and strain indicator.....	65
Figure 34: Stress-strain curves of the first set of parameters and wrought plate components using the Instron crosshead extension for yield and ductility .....	66
Figure 35: (a) Secondary electron micrograph from the parameter 1 tensile fracture surface images at 250x: <i>XY</i> orientation, (b) <i>ZX</i> orientation, (c) and wrought plate.....	68
Figure 36: Stress-strain curves of the second set of parameters and wrought plate components using strain gages and indicator.....	69

Figure 37: Stress-strain curves of the set of parameters and wrought plate components using the Instron crosshead extension for yield and ductility.....	69
Figure 38: (a) Secondary backscatter images of parameter 2 tensile fracture surface at 250x of the XY orientation, (b) ZX orientation, (c) XZ orientation.....	72
Figure 39: (a) Backscatter electron image of matrix in ZX orientation of parameter 2 tensile fracture surface, (b) EDS spectrum collected from the spot shown in (a). .....	74
Figure 40: (a) Backscatter electron image of matrix in ZX orientation of parameter 2 tensile fracture surface, (b) image of tensile specimen, (c) EDS spectrum collected from the spot shown in (a).....	75
Figure 41: Stress versus strain curve as given by the SURE-Pulse software. This is the stress-strain curve of specimen ZX-3 from the first set of process parameters. ....	76
Figure 42: (a) Secondary backscatter images taken at 50x on Charpy fracture surfaces: loose particulates from lack of fusion and defect cracks in the first parameter set ZX orientation and (b) a more acceptable fracture surface from the second parameter set ZX orientation .....	80
Figure 43: (a) Secondary backscatter images at 230x of second parameter Charpy fracture surfaces of XY, (b) ZX, and (c) XZ. ....	82
Figure 44: Crack propagation and defects in Charpy fracture surface from parameter set 2 in the XY orientation.....	82

## List of Tables

Table 1: Comparisons of some representative laser-based AM processes [1].....	3
Table 2: SLM printer process parameters into material, laser, scan, and environmental categories [44].....	7
Table 3: Renishaw Powder Chemical Composition [68].....	38
Table 4: Renishaw AM250 Specifications [7, 71, 72].....	42
Table 5: Two Sets of Printer Process Parameters .....	43
Table 6: ASTM E8/8M metric subsize standard for rectangular flat-bar tensile test specimen dimensions [51].....	48
Table 7: Omega Precision Strain Gage Characteristics .....	49
Table 8: XRF Chemical Composition by Weight Percentage of SS 316-L Powder .....	56
Table 9: Porosity results using ImageJ software and optical micrographs at 100x .....	63
Table 10: Brinell and Rockwell D test results on SLM printed 316L with two different process parameter sets and compared to reported wrought results. ....	64
Table 11: Tensile Properties of Parameter Group 1 and Wrought Plate Samples .....	67
Table 12: Tensile Properties of Parameter Group 2 and Wrought Plate Samples .....	70
Table 13: Split-Hopkinson compression results with different process parameters and print orientations then compared to wrought specimens. ....	77
Table 14: SHPB compression results at similar average strain rate values. ....	78
Table 15: Charpy V-notch results from both parameter groups .....	79

# Chapter 1: Introduction

## 1.1 Additive Manufacturing

Additive Manufacturing (AM) refers to manufacturing processes that adds a layer of material upon a previous layer until a 3D part is formed. 3D printing is a subset of AM in which the part is created from a computer-aided design (CAD) file by depositing or fusing a layer of material. It is considered a driving force of a “third industrial revolution” [1], along with digital manufacturing, since it has the potential to revolutionize manufacturing. This technology was first developed in the early 1980’s and was then commercialized in 1986 by 3D Systems with the release of the first stereolithography (SLA) machine. At this time the primary focus of AM was rapid prototyping (RP) [2]. However, with the expansion of printing technologies and materials in the years since, the ability to create functional parts has become the focus of experimental research and industrial application. Due to these advancements, AM’s ability to manufacture unique and complex designs, all while reducing material and tooling costs, has helped set it apart from traditional manufacturing.

AM materials include a variety of polymers, metals, and ceramics, although other materials are available in a depositable powder form of suitable particulate size ranges [3]. The expansion of materials has helped thrust AM into the spotlight and has helped further expand workable materials and the optimization of the processes.

Gibson et al. [2] defines eight steps in the AM process:

1. Conceptualize and CAD creation of part
2. Conversion to STL format
3. Transfer and manipulation of STL file on AM machine
4. Machine setup
5. Build
6. Part removal and cleanup
7. Part post-processing
8. Application

These steps are generally applicable to all AM platforms, however there can be variations depending upon the technology used and part design.

AM is broken down by machine classifications per ASTM F2792-12a: binder-jetting, directed energy deposition (DED), material extrusion, material jetting, powder bed fusion (PBF), sheet lamination, and vat photopolymerization [4]. Significant AM processes for metals include: Selective Laser Sintering/Melting (SLS/M), Laser Engineering Net Shaping (LENS), Laminated Object Manufacturing (LOM), Electron Beam Melting (EBM), Ultrasonic Consolidation (UC) [5], and Binder-Jetting (BJ). Below in Table 1 is a brief comparison of some of these systems [1].



Table 1: Comparisons of some representative laser-based AM processes [1]

<b>Process</b>	<b>Deposition mode</b>	<b>Layer thickness (<math>\mu\text{m}</math>)</b>	<b>Deposition rate</b>	<b>Dimensional accuracy (mm)</b>	<b>Surface roughness (<math>\mu\text{m}</math>)</b>
Direct metal laser sintering (DMLS)	Laser sintering	20-100	Depend on laser spot size, scan speed, and size, number, and complexity of parts	High, $\pm 0.05$	14-16
Selective laser melting (SLM)	Laser melting	20-100	ibid	High, $\pm 0.04$	9-10
Direct metal deposition (DMD)	Laser cladding	254	$0.1-4.1 \text{ cm}^3/\text{min}$	N/A	$\sim 40$
Laser engineered net shaping (LENS)	ibid	130-380	N/A	X-Y plane $\pm 0.05$ ; Z axis $\pm 0.38$	61-91
Directed light fabrication (DLF)	ibid	200	$10 \text{ g/min}$ ( $1 \text{ cm}^3/\text{min}$ )	$\pm 0.13$	$\sim 20$

### 1.1.1 Selective Laser Melting

Selective laser melting (SLM), or directed selective laser melting (DSLM), is a PBF process that uses a laser source in an inert atmosphere of nitrogen or argon to fuse particles on a substrate. This is accomplished by the laser scan selectively melting powder above its melting temperature [1]. Once the laser selectively melts the specimen slice, another layer is spread as the powder bed is lowered by that same amount, as shown in Figure 1 [6].

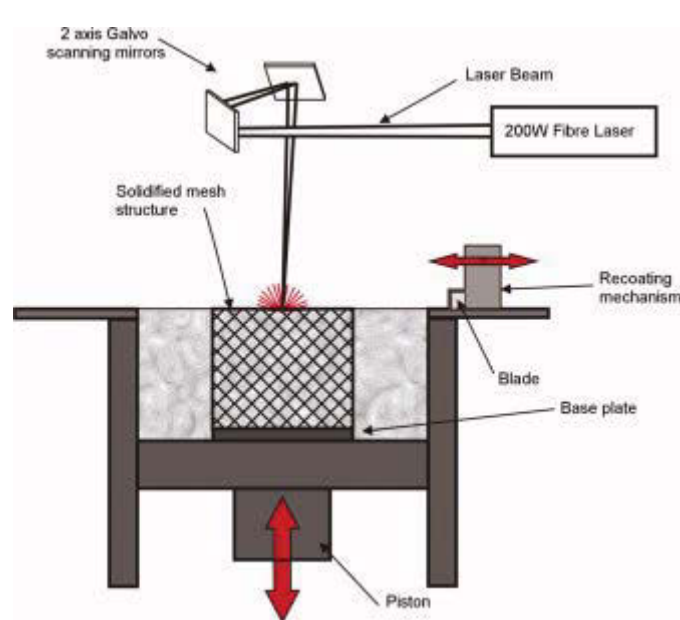


Figure 1: A typical SLM process schematic [6]

This process stems from the invention of the powder sintering technique developed by R.F. Householder in 1979, when he described his idea of sintering powders using a moving focused heat source with subsequent deposition and consolidation of powder layers. The moving heat source causes melting and joining of adjacent powder grains in the melt pool [7]. In 1995, SLM started in Germany at the Fraunhofer Institute

for Laser Technology ILT, while similar development occurred at Westinghouse Electric Corporation in 1988 and Sandia National Laboratories in the mid-1990's [1]. SLM machines are now commercially produced by companies such as Renishaw (MTT), EOS GmbH, Concept Laser GmbH, SLM Solutions GmbH, Realizer GmbH, and 3D Systems (Phenix) [8].

SLM is of particular interest to the aerospace [7, 9-11], medical [7, 9-12], automotive, electronic, tooling [7] industries, to name a few. The ability to manufacture an almost fully-dense part while eliminating tooling, severely lessening material costs, and reducing the need for post-processing is extremely attractive to industry. Of particular importance to medical and aerospace applications [7, 13] is the ability to manufacture foams and lattice structures [14] used for biomedical implants and weight reduction.

SLM materials that have been studied include cobalt-chromium alloys [6, 15], copper compounds [15], 24 karat gold [16], aluminum and aluminum alloys [1], titanium [1, 17] and titanium alloys [8, 13, 18-22], nickel-base superalloys [23], tool steels [7, 15, 24, 25], iron powders [25-31], and stainless steel alloys [9, 24, 33, 34], with ongoing research efforts focusing on expanding this list. Of note to this thesis are the previous investigations of stainless steel 316L [9-12, 14, 24, 25, 34-44]. These works utilize varying particulate sizes, AM technologies, and machine process parameters, in part because AM processes fall outside of most materials and process standards. For this reason the ASTM F42 Technical Committee on Additive Manufacturing Technologies was formed back in 2008 [2].

### 1.1.2 Process Parameters

The optimization of AM processes is a driving goal of research in the world of 3D printing. Experiments are designed to define a set of optimal process parameters and then characterize the material's properties and mechanical strengths. Single-bead [15, 34], single-layer [9, 24, 38], or density cube [6, 8, 10, 19, 20, 32] experiments are performed to determine a process formula that yields the best or desired density and surface quality. These experiments rely on density, melt pool morphology, and microstructure [8] to determine the optimal parameters, which are then utilized for a more complete build for further testing. This saves time and material on non-optimal builds that may have no use for industrial applications. Typical machine parameters that can be modified to determine optimal print parameters include: laser power ( $P$ ), laser scan speed or velocity ( $v$ ), laser scan or hatch spacing ( $h$ ), layer thickness ( $w$ ), laser point distance ( $d$ ), laser exposure time ( $t$ ), and scan strategy. Optimizations vary for the test material, particle size, atomization process, and machine components. A more comprehensive look at AM process parameters can be seen in Table 2 [44].

Table 2: SLM printer process parameters into material, laser, scan, and environmental categories (\* denotes alterable parameters) [44]

<b>Material</b>	<b>Laser</b>	<b>Scan</b>	<b>Environment</b>
Composition	Mode*	Scan speed*	Preheating*
Powder density	Wave length	Hatching space*	Pressure*
Morphology	Power*	Layer thickness*	Gas type*
Diameter of grains	Frequency*	Scan strategy*	O <sub>2</sub> level*
Distribution	Pulse width*	Scan sectors*	
Thermal properties	Offset*	Pulse distance*	
Flow properties	Spot size	Scaling factors*	

Scanning speed is the speed of the laser spot between heating points as shown in Figure 2a [7]. The exposure time (Figure 2b) between the particles and laser beam can be varied by changing the scan speed, which can results in varying final porosities of a printed part. The exposure time is how long the laser hits a particular point, and is usually between 0.5 and 25 microseconds. Using higher scan speeds has been shown to cause balling, which can cause the growth of dendrites. Typical scanning speeds range from

200 mm/s to 2000 mm/s [1]. The point distance (Figure 2c) is the distance between laser spots [7] and is often in the range of 10-50  $\mu\text{m}$ .

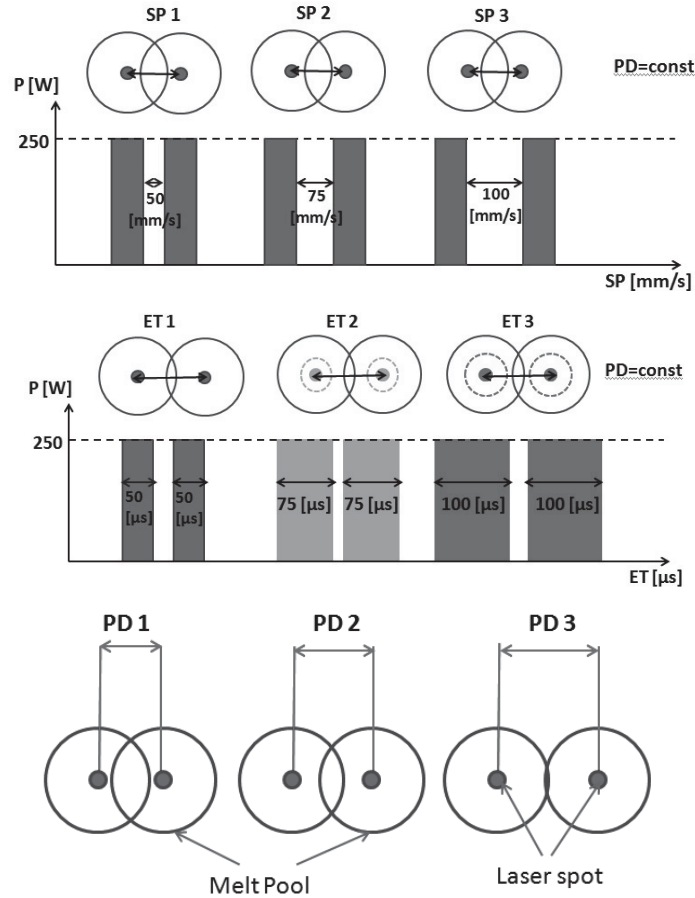


Figure 2: Schematics of scanning speed of the laser (a), exposure time of the laser (b), and point distance of the laser (c) [7]

The parameters shown above in Figure 2 are combined to define a term called laser density. This is a primary factor in affecting part density as well as material properties, which are determined by melt pool and grain characteristics. A linear laser

energy density term [1]  $\lambda$  (J/m) can be defined to estimate the laser energy input to melt a layer of material using laser power and scan speed.

$$\lambda = \frac{P}{v} \quad (1)$$

However, a 2D energy density term  $E_p$  (J/mm<sup>2</sup>) can be used, which adds the effect of hatch spacing. This form expands upon (1) by examining the total amount of energy that is absorbed by the powder bed as the laser scans. This is important in order to understand melt pool formation and characterization [2].

$$E_p = \frac{P}{v * h} \quad (2)$$

There are other process parameters that affect a SLM-produced part, most importantly layer thickness. Therefore, Simchi [25] defines a three-dimensional energy density term  $\psi$  (J/mm<sup>3</sup>) as shown in Eq. (3).

$$\psi = \frac{P}{v * h * w} \quad (3)$$

Cherry et al. [10] modify Eq. (3) such that it is defined using exposure time and point distance.

$$\psi = \frac{P * \frac{t}{h*d}}{w} \quad (4)$$

It has been reported that by combining scan strategies and high laser energy densities, it is possible to reduce significantly the volume fraction of defects [13]. An immersive study into the effects of scan strategies was done by Kruth et al. [27] in which six strategies (Figure 3) were investigated by measuring the deflection in the Z-direction.

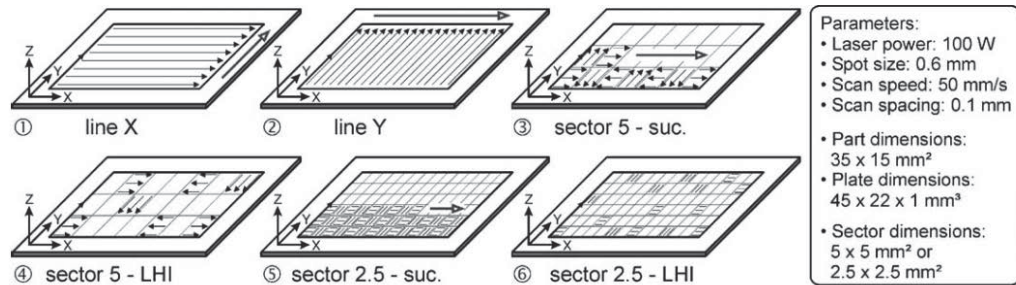


Figure 3: Six scan strategies tested by Kruth et al. [27]

In this study it was found that using sectioned scan strategies, the same melting behaviors and temperatures as the line X and Y strategies could be obtained using less laser energy density and in less time, resulting in fewer deformities. Beyond that, it was determined that the successive strategies (3 and 5) were preferable because of a lower thermal gradient.

Gong et al. [8] used an alternating scan strategy in which the laser scans in one direction on even layers and perpendicular to that direction on odd layers. The Ti-6Al-4V parts using this strategy, combined with other parameters, were deemed not suitable due to porosity that was likely due to the melt pools being less than the layer thickness. This strategy was also used by Simchi [25] and Simchi and Pohl [29], who compared the alternating strategy to normal line X and line Y scanning. A conclusion of their studies was that the biggest effect scan strategies has is on the development of thermal stresses.

Zhou et al. [6] used two different scan strategies on cobalt chrome in order to recommend a texture controlling method. The first scan strategy rotates the scan angle by  $0^\circ$  each layer and is called “zigzag”, while the second rotates the angle  $67^\circ$  each layer and is called “cross-hatch.”



Columnar grains growing epitaxial from grains in previous layers was a result of the zigzag strategy, while the cross-hatch strategy caused a more complex and varied melt pool. The cross-hatch strategy is also known as the meandering path strategy and was used by Cherry et al. [10] and Brown [33]. A schematic of the meandering strategy is shown below in Figure 4. It is one of the simplest patterns as each layer is rotated and translated to prevent the same points from being exposed multiple times, thus ensuring a better density.

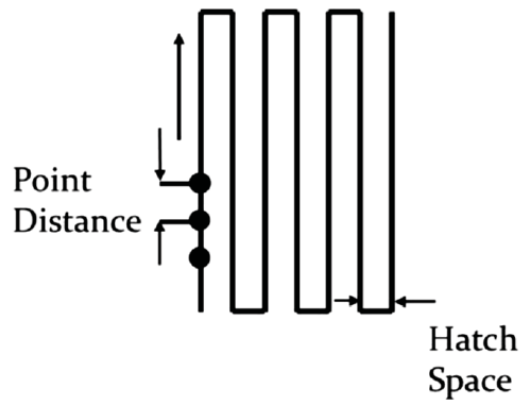


Figure 4: Schematic of a single layer meandering scan strategy [10]

Qui et al. [19] used a strategy in which the build is divided into a number of squares called “islands” scanning. In this strategy islands are randomly scanned, and the scan direction of the neighboring island is rotated by  $90^\circ$ , as shown in Figure 5. After the entire layer is scanned, a contour line around the build border is scanned to improve surface qualities. Yasa and Kruth [34] and Qui et al. [20] also used the island scanning strategies.

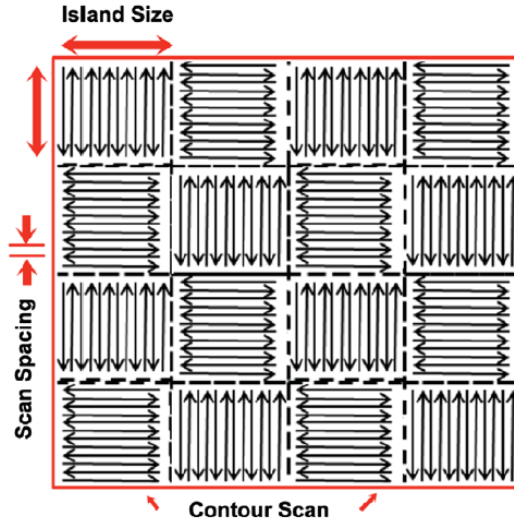


Figure 5: Islands scanning strategy [19]

Tolosa et al. [37], among others, have shown that 3D printed parts to have anisotropic properties, meaning properties depend on the manufacturing orientation. Parts printed in the  $XY$ -plane (flat) typically have stronger tensile properties because loads are parallel to the build layers, while parts printed in the  $ZX$ -plane (vertical) have the build layers pulled apart by such loads. Qui et al. [19] concluded that the anisotropy of their parts is due mainly to the orientation of columnar grains and differences in thermal histories.

Simchi [25] found that as the laser energy input increases (higher laser power along with lower scan speed, hatch spacing, and layer thickness), the density increases. Cherry et al. [10] supported this, and also showed that point distance has a larger effect on surface roughness, increasing with increased point distance, than exposure time. Studies show that variations in a process parameter affects either the microstructure, density, or mechanical properties of a printed part.

Extensive testing has been done to attempt to determine optimal process parameters for varying machines and materials, and for that reason, experimental methods are frequently introduced to speed up this progression. Paul et al. [45] used the Taguchi method in order to evaluate several design parameters of laser rapid manufacturing (LRM) simultaneously with fewer experiments. Their aim was to modify laser power, scan speed, and powder feed rates to determine the optimal parameters for a max deposition rate, as LRM uses a laser to melt raw feed materials such as powder or wire. Others, such as Brown [33], follow the design of experiments (DOE) format to speed up the optimization process.

### 1.1.3 Post-Processing

While SLM has shown the ability to produce near-full dense parts approaching 99.9% density without post infiltration, sintering, or hot isostatic pressing (HIP) [1], there has been fairly extensive research on possible improvements with the addition of post-processing. While it is considered a strength of PBF parts, and SLM parts in particular, to not require post-processing, there are still possible treatments to improve printed specimens, especially in unique and specialized applications.

One such investigation examined the potential benefit of laser re-melting for enhanced surface quality and residual porosity, reported by Yasa and Kruth [34]. Laser re-melting attempts to improve traditional SLM by rescanning the layer a second time before another layer of powder is spread. Results show a significant reduction of process-induced porosity (from 0.77% to 0.036%) and decrease in surface roughness from 12  $\mu\text{m}$  to 1.5  $\mu\text{m}$ .

Another post-processing study attempted to determine the differences in mechanical strength between as-built and stress-relieved Ti-6Al-4V tensile samples, done by Simonelli et al. [13]. They concluded that the stress relief heat treatment alters the phase composition and affects the tensile properties, most visibly in terms of elongation. They claimed that stress relief might be needed to eliminate distortion due to large residual stresses. Work by Leuders et al. [46] agrees with that claim, as heat treatments and HIP treatments on SLM Ti-6Al-4V increased elongation by reducing residual stresses inherent to the manufacturing. This increased the volume fraction of the  $\beta$ -phase and changed grain microstructures. Yasa et al. [31] determined that heat treatments on SLM maraging steel 300 increased the hardness and ultimate tensile strength values, but at the cost of decreased impact toughness and elongation. Vrancken et al. [21] investigated varying annealing temperatures and water quenching treatments on SLM printed Ti-6Al-4V with added Mo and found that the hardness values remained unchanged between quenching temperatures and were in line with wrought, although other mechanical properties suffered in comparison to other SLM printed titanium alloys.

Comparatively, Riemer et al. [38] determined that stress relieving heat treatments had no significant effect on monotonic properties of 316L. This is due to the lack of phase transformations during cooling as experienced with Ti-6Al-4V. Riemer et al. also explored the effects of HIP post-processing to reduce porosity for compact tension specimens and the HIPed specimens had better fatigue results than as printed, and within range of traditionally processed 316L. It was found that turning the surface to remove surface roughness improved mechanical values in both cyclic and monotonic tests.

Trelewicz et al. [12] are considering heat treatments in future investigations of the corrosion resistance of 316L.

## 1.2 Microstructural Analysis

Microstructural properties of AM-processed parts are two-fold: the exterior surface microstructure and interior grain microstructure [1]. This includes surface roughness, typically caused by balling phenomena, and grain characterization. Therefore, it is the goal of nearly every PBF investigation to try to optimize process parameters in order to achieve the desired microstructure and density of the printed material. Grain structure and size is a specific concern to PBF because of the rapid melting, cooling, and solidification of particulates. Ideal cooling of particulates is related to section thickness, which in this case is representative of the PBF procedure and can be simply related in (5). Under the conditions of non-equilibrium cooling relationships in traditional manufacturing processes, there is a relationship between the cooling rate ( $\dot{T}$ ) and both primary and secondary dendrite arm spacings. Since primary dendrites can happen anywhere in the melt, secondary dendrite arm spacings are more easily related to cooling rates, using material constants  $n$  and  $K$  as seen in (6) [47].

$$\dot{T} = 10^4 z^{-2} \quad (5)$$

$$\lambda = K\dot{T}^{-n} \quad (6)$$

For laser additive manufacturing, Hofmeister et al. [48] defined the cooling rate for melt pools in laser processing in (7). This equation includes powder absorptivity at the laser wavelength ( $\alpha_\lambda$ ) and diameter of the melt pool ( $\delta$ ), as well as material constants:

density ( $\rho$ ), thermal conductivity ( $\kappa$ ), and specific heat conductivity ( $c$ ). This equation was simplified by Ma et al. [28] in (8) where  $C$  is a new cooling rate constant of the molten pool that is proportional to the powder material and laser power density.

$$\dot{T} = \frac{\alpha_{\lambda} P v^{1/2}}{\delta^2 (2\rho c \kappa)^{1/2}} \quad (7)$$

$$\dot{T} = C E_{\rho} \sqrt{\frac{v}{w^3}} \quad (8)$$

Energy densities and cooling rates directly affect the mechanical properties as well as part microstructures, defects, and densities. Because density is a major obstacle facing any AM process, any investigation involving 3D printing uses a method to determine part density whether it is computed tomography (CT) scanning, optical microscopy (OM) imaging, or employing the Archimedes method (9). In the Archimedes method a part is weighed once in dry air and then again suspended in a fluid, typically de-ionized water, so that the part density can be calculated using (9) [11]. SLM investigations for 316L have yielded densities over 99% [11], up to 99.9% [36].

$$\rho_{part} = \frac{m_{air}}{m_{air} - m_{fluid}} * \rho_{fluid} \quad (9)$$

Specimen density is directly affected by inherent defects and process parameters. Majumdar et al. [36] reported that increasing laser scanning speeds reduces the area fraction of porosity in SLM printed 316L, while area fraction porosity is independent of applied laser power. Yadroitsev and Smurov [9] reported that with increases in scanning speeds and layer thicknesses, pores became more oriented (elongated and perpendicular to sintering direction) and surface roughness was increased. In an earlier study, Yadroitsev and Smurov [15] stated that instabilities in 316L single tracks appear in the

form of distortions and irregularities at low scanning speeds and the balling effect at excessively high speeds. However, they determined that a range of optimal scanning speeds was larger for higher laser powers. Li et al. [35] also found irregularities in the form of pores caused by the balling effect in SLM printings of 316L at lower laser powers and higher scan speeds. Balling is when a molten track possesses a high viscosity or wetting angle so that a large number of agglomerates or balls form a rough surface or in porous areas, as in Figure 6. Furthermore, Li et al. determined that gas atomized powder possessed a denser structure than water atomized parts due to lower oxygen contents. Another conclusion was that regularly shaped pores were caused by wider hatch spacing and that densification could be improved by increasing the overlap ratio of scanning tracks, which would also diminish micro-cracks caused by large stress fields and temperature gradients. Cherry et al. [10] found the balling effect at both high and low energy densities, with small balls dominating at low energy density and a mixture of small and large at high energy density.

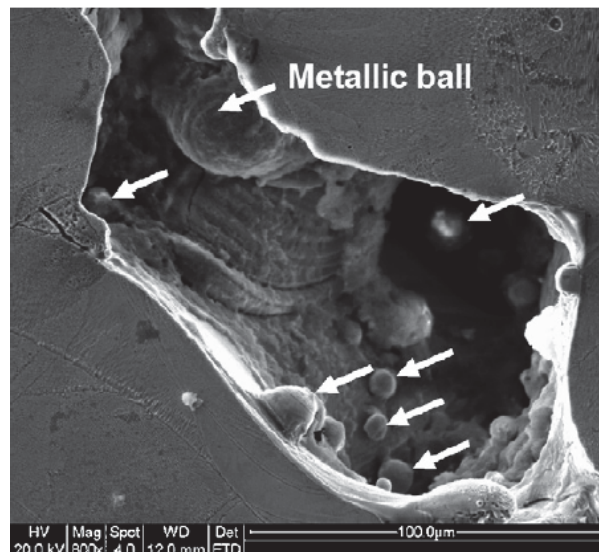


Figure 6: SEM image of polished section with a balling induced pore by Li et al. [35]

With use of OM and SEM imaging, microstructures can be determined. Yasa and Kruth [34] found fine cellular/dendritic structures in SEM images of SLM printed 316L. This is due to rapid solidification due to very high cooling rates and is a common microstructure obtained by laser processing techniques [10, 34]. Work done with 316L by Kruth et al. [49] claims that secondary dendrite arm spacing below 1  $\mu\text{m}$  is a feature characteristic of high strength. Similar microstructures were examined by Ma et al. [28], where the cellular dendrites spacing grows with increasing layer thickness. However, images taken by Yasa and Kruth [34] revealed that a higher number of scans in re-melting leads to finer lamellar structures.

While Trelewicz et al. [12] performed research on the corrosion resistance of SLM printed 316L, they also did extensive microstructural work including XRF, XRD, chemical etching, and microscopy (OM and SEM). Parts were etched using Vilella's reagent, which exposed a heterogeneous microstructure with a network of melt pools aligned in a weave-like pattern. This is due to the laser-scanning pattern and rapid solidification of the layers. While at lower magnifications aligned melt pools were observed in OM micrographs, at higher magnifications cell boundaries (from etching) such as those in Figure 7 were seen. Elemental analysis using energy dispersive x-ray spectroscopy (EDS) on these cell boundaries show an enrichment of molybdenum (Mo), which is etchant resistant due to its corrosion properties. A transmission electron microscopy (TEM) sample was extracted using focused ion beam (FIB) milling. Under TEM examination elongated grains were observed, and both bright and dark field images revealed a non-equilibrium microstructure.



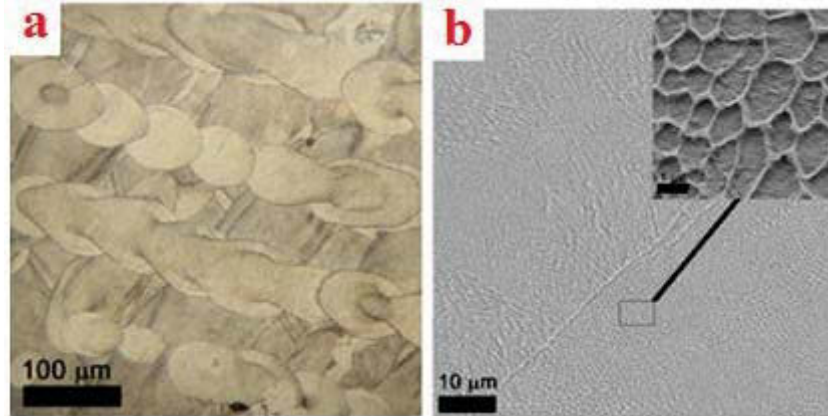


Figure 7: (a) Optical micrograph of grain boundaries in 316L etched with Vilella's reagent; (b) SEM image of the cellular structure at the intersection of two misaligned melt pools [12]

While microscopy can determine the microstructures and grain properties of a printed structure, it is only one step in the optimization and characterization of AM processes and parts. Microstructures can help researchers infer how a part might react to mechanical situations, but AM has new issues to be taken into account, such as rapid solidification and cooling. Therefore, even with a desired microstructure, it is imperative that AM specimens are mechanically tested and compared to both traditionally manufactured parts and other AM parts for industrial application worthiness determinations. Such measures are required for AM to expand its use beyond rapid prototyping (RP).

### 1.3 Mechanical Testing

Gu [1] notes that the key to the mechanical properties of AM-processed parts is the solidification microstructure. Mechanical testing is performed on AM specimens, often after optimized process parameters have been determined, to test homogeneity and to

compare mechanical strengths against traditionally manufactured samples. In this way AM processes and parts can be considered acceptable for industry applications. Typical mechanical tests performed on AM specimens include hardness, tensile, compression, fatigue, fracture, bending, and high strain rate examinations.

### 1.3.1 Hardness Testing

Hardness is a material's resistance to permanent indentation, although it can also be defined as its resistance to scratching or wear. It is not considered a fundamental property since it depends on the shape of the indenter and the load applied. The most common standardized hardness tests include Brinell, Vickers, Knoop, and Rockwell, the characteristics of which can be seen in Figure 8 [50]. Hardness testing is used in AM as a first indication for the uniformity of mechanical properties [28] and, therefore, is a common mechanical test in AM research.

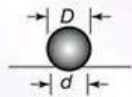



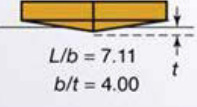
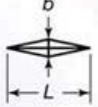
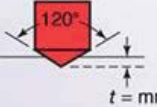

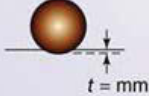

Test	Indenter	Shape of indentation		Load, P	Hardness number
		Side view	Top view		
Brinell	10-mm steel or tungsten carbide ball			500 kg 1500 kg 3000 kg	$HB = \frac{2P}{(\pi D)(D - \sqrt{D^2 - d^2})}$
Vickers	Diamond pyramid			1-120 kg	$HV = \frac{1.854P}{L^2}$
Knoop	Diamond pyramid			25 g-5 kg	$HK = \frac{14.2P}{L^2}$
Rockwell					
A } C } D }	Diamond cone			60 kg	HRA
				150 kg	HRC
				100 kg	HRD
B } F } G }	$\frac{1}{16}$ - in. diameter steel ball			100 kg	HRB
				60 kg	HRF
				150 kg	HRG
E	$\frac{1}{8}$ - in. diameter steel ball			100 kg	HRE

Figure 8: General characteristics of hardness testing methods [50]

Since both hardness and tensile strength are indicators of plastic deformation resistance, it is possible, and also desirable, to relate them according to (10) where  $HB$  is the Brinell hardness value. It must be noted that this relation does not hold for all materials [52].  $HB$  can be calculated using the equation seen in Figure 8.

$$TS (MPa) = 3.45 * HB \quad (10)$$

Ma et al. [28] performed microhardness tests on horizontal and vertical sections of 1Cr18Ni9Ti stainless steel samples. On the horizontal sections the microhardness ranges from ~235-265 HV, which decreases with layer thickness. In the vertical sections the microhardness decreases from 260 to 220 HV with layer thickness. It is claimed that the microhardness shows directional dependence due to anisotropy of the microstructure.

Paul et al. [45] evaluated the hardness of LRM produced Inconel 625 using the Rockwell hardness test. The hardness of the LRM parts as fabricated was higher (46-52 HRc) than solution annealed (27 HRc), though LRM samples that were annealed (29-30 HRc) were more comparable to conventionally processed Inconel 625. Similar results are reported by Santos et al. [17] for pure titanium. The hardness of the AM produced parts increases with peak power and were greater than wrought due to oxygen pickup and titanium carbide precipitation, although values decreased after annealing. Vrancken et al. [21] found that the Vickers microhardness of the material with added Mo ( $338\pm 5$  HV) was not as hard as SLM printed Ti-6Al-4V ( $399\pm 5$  HV); however, heat treatments followed by water quenching improved those results to ( $468\pm 7$  HV at  $650^{\circ}\text{C}$ ). Higher temperature treatments did not add to the hardness and were almost exactly identical to the as-built measurement:  $338\pm 6$  at  $850^{\circ}\text{C}$ ,  $331\pm 8$  at  $900^{\circ}\text{C}$ , and  $336\pm 4$  at  $1050^{\circ}\text{C}$ . They attribute the high hardness value at  $650^{\circ}\text{C}$  to the higher percentage of the  $\alpha$ -phase that was diminished at higher temperatures due to hardening.

Tolosa et al. [37] performed Vickers hardness tests along each one of their orientation case SLM 316L samples and found results (average of 235 HV) that are homogeneous and similar to those of wrought specimens. Similar SLM 316L Vickers hardness results were reported by Cherry et al. [10]. They reported a maximum mean of 225 HV on the max dense (99.62%) specimens, showing a relationship of decreasing hardness values with increasing porosity due to pores collapsing under load.

### 1.3.2 Quasi-Static Tensile Testing

Tensile testing is the most common test for determining the strength-deformation characteristics of materials, in part due its relative simplicity [50]. Through a simple tensile test, following ASTM E8/8M [51], it is possible to determine that quasi-static Young's modulus ( $E$ ), 0.2% yield strength ( $\sigma_y$ ), ultimate tensile strength (UTS), and elongation values. From this a lot of information can be gleaned, including whether a material is brittle or ductile. The Young's modulus is determined by taking the slope of the elastic zone of a specimen's stress versus strain curve, although it can also be solved using Hooke's Law (11).

$$E = \frac{\sigma}{\epsilon} \quad (11)$$

The yield strength is determined by offsetting a straight line parallel to the elastic region at a specified strain--typically 0.002. The UTS is the maximum stress value on a stress versus strain curve. Both of these determinations are seen in Figure 9 [51].

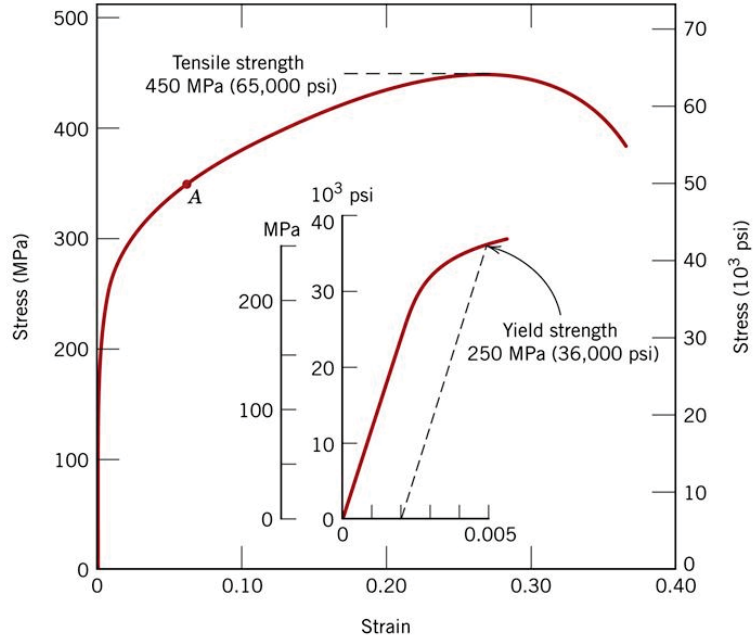


Figure 9: Stress-strain curve demonstrating how to determine ultimate tensile and 0.2% yield strengths [51]

Ductility is the strain in a specimen at fracture and can be determined by either calculating elongation (12) or reduction of area (13). Elongation is the difference in initial versus final gage lengths, while reduction of area is the difference between initial and final gage cross-sectional areas [50].

$$Elongation = \frac{l_f - l_o}{l_o} * 100 \quad (12)$$

$$Reduction\ of\ Area = \frac{A_o - A_f}{A_o} * 100 \quad (13)$$

With the relative ease of producing standardized tensile specimens and results as well as the wealth of material properties collected, it is not surprising that it is a popular method of testing AM parts. Tensile tests from powder bed fusion and directed energy deposition in materials such as stainless steels, titanium alloys, nickel superalloys, and

cobalt chrome have been performed. Typically the goal is to determine how varying orientations or printer parameters affect material performance.

Yadroitsev and Smurov [15] produced SLM printed tensile specimens of 316L and CoCr that showed that both materials had comparable ultimate strengths, significantly higher yields, and much lower elongations than their wrought counterparts. Paul et al. [45] also showed that AM Inconel 625 had better yield and UTS results with comparable elongations, while utilizing a different 3D printing technology and not being affected by rastering angle.

Simonelli et al. [13] examined the effects of orientation and stress relieving of Ti-6Al-4V printed on a Renishaw AM250 with optimized process parameters. Tensile specimens were printed directly as standard dog bones, rather than printing bulk material to be machined later, in three orientations (flat, vertical, edge). It was determined that elongation was affected by printing orientation, but  $E$ ,  $\sigma_y$ , and  $UTS$  were not adversely varied shown in Figure 10. A similar study was done by Yadroitsev and Smurov [15], who produced SLM Inconel 625 samples by machining them from rectangles printed parallel and perpendicular to the substrate and at angles of  $0^\circ$ ,  $45^\circ$ , and  $90^\circ$  to the scanning direction. The Young's modulus was greatly affected by orientation, with the horizontal results being 1.5 times larger, but not by the angle of scanning direction. The other mechanical properties were homogeneous and better than wrought Inconel 625 for yield and ultimate strengths.

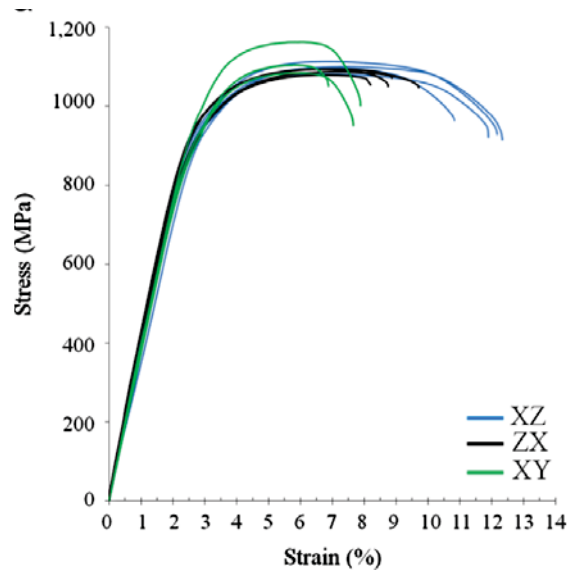


Figure 10: Stress strain curves of AM produced Ti-6Al-4V tensile specimens printed in three orientations [13]

Vrancken et al. [21] tensile tested Ti-6Al-4V samples with added Mo and post-processed, where it was shown that compared to SLM Ti-6Al-4V the elongation was increased while the UTS, yield, and elastic modulus were decreased. Leuders et al. [46] investigated the effects of post-processing (heat treatments and HIP) on Ti-6Al-4V samples and showed similar results for UTS, yield, and elongation due to the post-processing, mostly due to an increase in the  $\beta$ -phase.

Ma et al. [28] performed tensile tests on SLM printed 1Cr18Ni9Ti austenitic stainless steel specimens of two orientations, flat and vertical, using varying layer thicknesses. Results show that with increasing layer thickness, the mechanical strengths trend down while the elongation trends up. This is explained by the higher cooling rate achieved using thinner layers and higher laser energy densities. The tensile results were anisotropic with the XY samples having superior tensile properties due to the load being parallel to the build layers and perpendicular to the cellular dendrites. Tolosa et al. [37]



SLM printed 316L tensile specimens in a wide assortment of orientations and used the results to determine optimum print angles. The samples showed anisotropy, and the results depended on print orientation. However, it was shown that the mechanical properties of the printed specimens were higher than the rolled wrought counterparts, especially the yield strengths, all while maintaining good elongation.

Tensile studies have also been done with specimens produced by directed energy deposition (DED). An early study of SS 304 tensile specimens printed under three different process conditions, where each condition also contained three different deposition angles, was done by Kahlen and Kar [53] to compare the effects of laser power and powder delivery rate. In all cases the ultimate strengths achieved by the printed material did not meet the nominal UTS of wrought 304, although in three of nine cases the printed material met the yield strength of the wrought. It is claimed that the small time scales for solidification (causing residual stresses) and larger melt pools contribute to these results.

Results of a 316L laser rapid manufacturing (LRM), a form of DED, study by Ganesh et al. [43] showed UTS and elongation results in line with other SLM studies, as well as cast, wrought-cold finished, and wrought-hot finished-annealed. However, the yield stress was reported lower than previously shown by SLM, 250-275 MPa versus 328-344 MPa, but similar to the traditionally manufactured results. Elongation results fell in the range of previous SLM results, and were attributed to microporosity and oxide inclusions due to the manufacturing process. LRM Inconel 625 samples were tensile tested with UTS lower and yielded higher than other reported LRM and traditionally manufactured values, per Ganesh et al. [54].

### 1.3.3 Split-Hopkinson Compression Testing

Typical material properties, like those listed previously, are obtained under quasi-static loading conditions that are unable to test high-rate loading conditions. Split-Hopkinson pressure bars (SHPB) are used to characterize the mechanical response of materials deforming at high strain rates ( $10^2$ - $10^4$  s<sup>-1</sup>) [54]. Kolsky [55] explained the need for high-strain rate testing in engineering due to the dependence of material properties on the rate at which stresses are applied and in physics due to the relationship between physical problems and molecular structure. In 1949 he introduced the pressure bar to research high-strain rate compression phenomena in polythene, rubber, Perspex (polymethyl-methacrylate), copper, and lead. Kolsky found that the metals were permanently deformed and that the difference in their response resulted from the difference in their yield points.

SHPB can now perform not only high strain rate compression tests, but also those in tensile and torsion. In order to avoid overlapping wave pulses from the incident and transmission bars, it is recommended that the incident bar be two times longer than the transmission with the specimen placed between them (Figure 11). Whereas original Kolsky bars captured information by means of setup of amplifiers, condenser microphones, and oscillographs, newer configurations utilize a high resolution data acquisition system and computer.

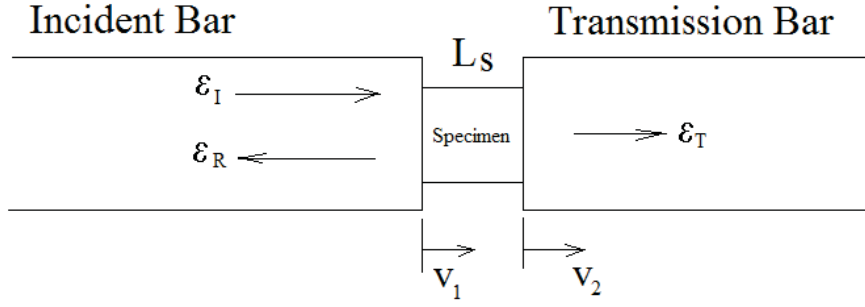


Figure 11: Split-Hopkinson pressure bar setup for a compression specimen, where it is important to note that the specimen diameter is smaller than the bar diameters [55]

The stress ( $\sigma_s$ ), strain ( $\epsilon_s$ ), and strain rate ( $\dot{\epsilon}_s$ ) in the specimen can be calculated using the wave signals recorded in the incident and transmission bars. These are given by (14-16) below where  $E$  and  $C_0$  are the Young's modulus and elastic wave velocity of the bars, respectively;  $L$  is the initial specimen length;  $\frac{A_b}{A_s}$  is the cross-sectional area ratio of the bar and specimen; and  $\epsilon_t$  and  $\epsilon_r$  are the transmitted and reflected wave signals, respectively [57].

$$\sigma_s = E \left( \frac{A_b}{A_s} \right) \epsilon_t \quad (14)$$

$$\epsilon_s = \left( \frac{-2C_0}{L} \right) \int_0^t \epsilon_r dt \quad (15)$$

$$\dot{\epsilon}_s = \frac{d\epsilon_s}{dt} = \left( \frac{-2C_0}{L} \right) \epsilon_r \quad (16)$$

The transmitted and reflected wave signals can be calculated from the bar velocities along with the incident wave signal ( $\epsilon_i$ ) as seen in Figure 11 and are shown in (17-19) [55], although they are typically measured by strain gages attached to the transmission and incident bars.

$$\varepsilon_t = \left( \frac{v_2}{C_0} \right) \quad (17)$$

$$\varepsilon_i = \left( \frac{v_{st}}{2C_0} \right) \quad (18)$$

$$\varepsilon_r = \varepsilon_i - \left( \frac{v_1}{C_0} \right) \quad (19)$$

The specimen yield is calculated in (21) using the elastic strain energy ( $E_B$ ), which for linear elastic bars is shown in (20).

$$E_B = \rho_B C_0^2 \quad (20)$$

$$\sigma_y = \left( \frac{A_b}{A_s} \right) E_B \varepsilon_t \quad (21)$$

While accurately determining stresses (ultimate and yield) can be accomplished using the SHPB, the rate-independent Young's modulus of alloys are usually measured only 30-50% of their quasi-static measurements due to the inaccurate measurement deformation [55].

It is important to note that there is no standard approach available at present for SHPB experiments, similar to the lack of standardization of AM [55]. Available research into high strain rate testing of AM materials appears to be limited, although work with other high strain rate impact testing has been done on AM 316L. Winter et al. [58] fabricated 316L cellular structures and used a gas-gun-driven flyer to do impact experiments at rates varying between  $300 \text{ ms}^{-1}$  and  $700 \text{ ms}^{-1}$ . Similar work was reported by Gray et al. [40] with DED manufactured and DED heat treated parts versus wrought plate, which preliminary positive results.

However, there have been investigations into powder metallurgy stainless steel 316L specimens. High strain rate testing of 316L is important due to its uses in aerospace [57], automobile [57], defense [57], and nuclear [57, 59, 60] applications where parts may be subjected to high speed collisions or explosions [60]. Lee et al. [57] compared the compression results of three relative sintered densities (83, 88, and 93%) of SS 316L under different quasi-static and dynamic strain rates. The samples were traditionally sintered using 13  $\mu\text{m}$  particles. It was determined that the mechanical behavior of 316L is sensitive to both strain rate and sintered density, as shown below in Figure 12 [57].

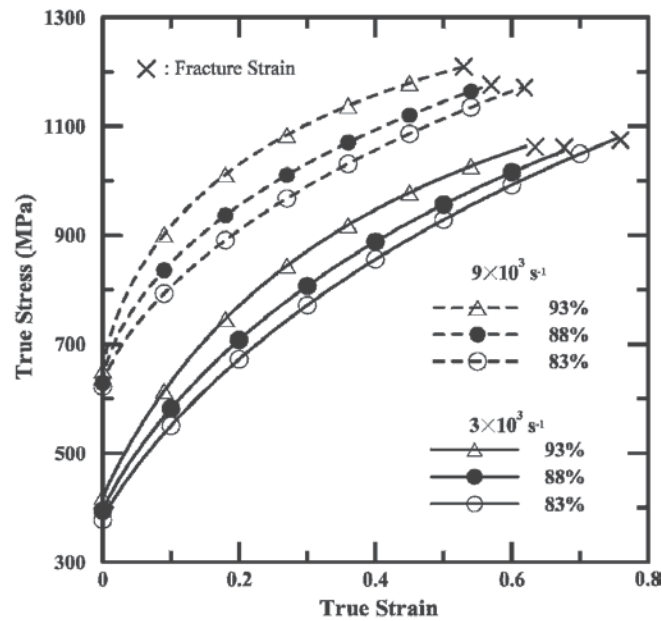


Figure 12: Lee et al. results of quasi-static and SHPB compression testing of different density 316L samples at different strain rates [57]

Lee et al. [59] examined the strain rate effects on sintered 316L specimens (96% dense) using quasi-static and dynamic strain rates. It was determined that for increasing strain rate, the yield strength increased while the strength and work-hardening coefficients decreased. It was also shown that at high enough strain rates, fracture

occurred due to plastic instability and that the specimens failed in a ductile mode. Another study examined the high temperature effects on sintered 316L samples at different strain rates, performed by Lee et al. [60]. This study yielded results that show that the yield strength and work coefficient increase with increasing strain rate, but decrease with increasing temperature, implying sensitivity to both factors.

#### 1.3.4 Charpy V-Notch Impact Testing

ASTM E370 defines the Charpy V-notch impact test as a dynamic test in which a notched specimen is struck and fractured in a single blow by a testing machine. The measured values resulting from this test method include energy absorbed, percentage shear fracture, and lateral expansion opposite of the notch [61]. Charpy testing is done to get an indication of impact resistance against stress concentration and resistance against crack propagation [45]. Good toughness results tend to result from a good mixture of mechanical strength and ductility.

Paul et al. [45] investigated the effects of rastering orientation ( $0^\circ$ ,  $90^\circ$ , and mixed) of Inconel 625 manufactured by LRM. The results were homogeneous across the orientations and on par with hot-finished and annealed Inconel 625 and fractured in a ductile mode. Vrancken et al. [21] tested two orientations (horizontal and vertical) of solution-treated SLM Ti-6Al-4V + 10Mo. They found that the energy absorption was significantly lower than had been reported for SLM Ti-6Al-4V, and it was reported that the horizontally built specimens absorbed twice as much energy as the vertically built ones. They claim that this is due to the crack front growing parallel to the building

direction in the horizontal samples, while in the vertical direction, the crack growth occurs in between build layers, which results in the smoother fracture surface seen below.

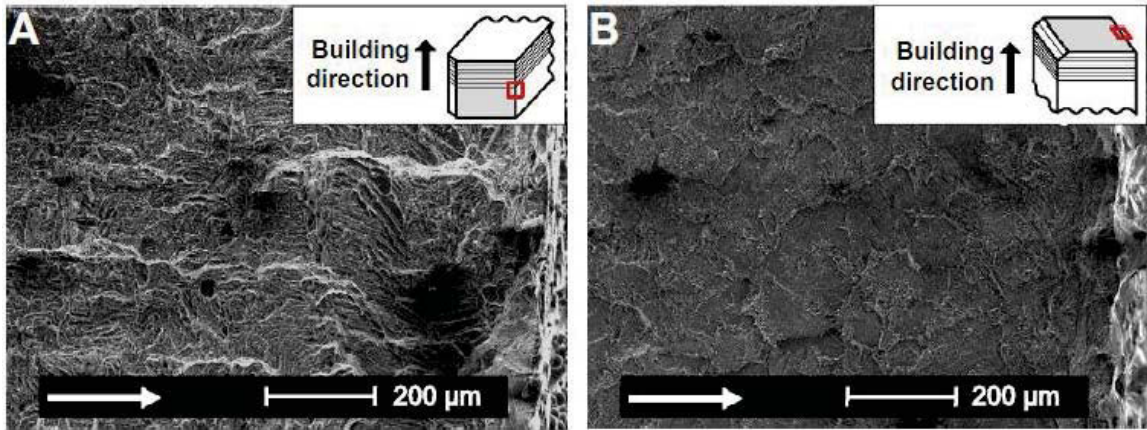


Figure 13: Fracture surfaces of SLM produced Ti-6Al-4V+10Mo Charpy V-notch specimens. The white arrows indicate crack growth direction with the insert showing build direction [21].

Tolosa et al. [37] produced specimens in two orientations according to the best and worst tensile results ( $30^\circ$  in the XY plane and  $0^\circ$  in ZX plane) previously collected. The 316L parts in the ZX plane (50 J) performed significantly worse than those in the XY plane (63 J), but both were lower than wrought results ( $<75$  J). Santos et al. [17] also found SLM printed samples to perform worse than conventionally processed samples, in this case for pure titanium. They attribute the low impact results to porosity and impurities within the printed material. Ganesh et al. [43] tested LRM 316L samples printed both along and against the material build-up directions. Print direction did not have an effect as all results were between 90-110 J, close to reported results of 105 J for traditionally manufactured 316L. Specimens of both directions exhibited columnar facets along the crack growth which proves that that fracture occurred along preferred

crystallographic planes. Microscopy showed mixed modes of fracture, as there were dimple and cleavage-like facets.

Yasa et al. [31] tested printed maraging steel 300 specimens as built on two different SLM machines and also specimens heat-treated with optimized aging conditions. The as-built samples had higher impact toughness results than the heat-treated and traditional annealed samples, although the traditionally manufactured samples were tougher than the AM treated samples.

### 1.3.5 Fracture and Fatigue Testing

Fracture and fatigue testing procedures typically follow ASTM standards E647 [62] and E1820 [63]. Fatigue crack growth rate (FCGR) and fatigue toughness are important to study in order to clarify the integrity and estimate the safe life of structural parts. Fatigue crack propagation results are needed to assess safe lives of products, of importance to industrial applications. Fracture toughness is an empirical material property describing the effect of defects on the load-bearing capacity of a part [43]. This is particularly important for biomedical implants which undergo cyclic loading [37]. There are three modes of fracture (Figure 14): symmetric loading or opening mode (mode I), antisymmetric loading or shearing mode (mode II), and mixed or tearing mode (mode III). While a specimen may fracture under a critical load, a specimen can also fail under cyclic loadings of magnitudes below the failure load after a number of cycles. This failure is known as fatigue [64]. Compact tension (CT) testing is a standard for studying either phenomena. Values that can be determined from compact tension testing include: stress intensity factor ( $K$ ), strain energy release rate term J-integral ( $J$ ), and crack-tip



opening displacement (*CTOD*). The stress intensity factor depends on specimen geometry, crack size and location, and load magnitude and mode (22).

$$K = f\sigma\sqrt{\pi a} \quad (22)$$

Equation 18 serves to determine the stress intensity factor for a simple case where  $f$  is the geometry factor for the specimen and defect,  $\sigma$  is the applied stress, and  $a$  is the defect size [65]. The J-integral value helps to predict when a crack should propagate and can compute the stress energy release rate. Structure failure can be predicted from the CTOD value, and when CTOD value reaches a critical value, the crack begins to propagate [66].

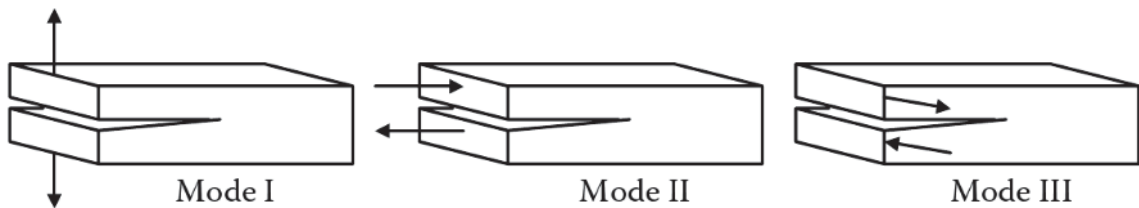


Figure 14: Three modes of loading relative to a crack [64]

High-cycle fatigue (HCF) and CT tests were done on SLM Ti-6AL-4V printed in two orientations by Leuders et al. [46]. The HCF regime was chosen to evaluate the effect of heat treatments on the fatigue strength of SLM-processed cylinders, and the results show that the fatigue life was greatly increased with the post-processing. It was shown that the stress-concentrating porosity of the samples most greatly affected the fatigue results since the HIPed samples, as they did not fail in the fatigue tests (interrupted at  $2 \times 10^6$  cycles). Using the staircase method, the HIPed samples demonstrated an estimated 620-630 MPa fatigue limit, within the range (392-620 MPa) of conventionally processed titanium alloys. However, the CT crack growth is most

heavily affected by the reduction of residual stresses, added volume of the  $\beta$ -phase, and modified grain structure due to the post-processing. The threshold values after treatment were all similar to those reported for conventionally processed Ti-6Al-4V. Work done by Vrancken et al. [22] also determined that residual stresses, mainly oriented along the building direction, affects fatigue properties of SLM printed Ti-6Al-4V, and that stress relief treatments can positively affect FCGR behavior.

Riemer et al. [37] followed a similar set of tests as [46] on SLM printed 316L. However, due to the microstructure achieved during the SLM process, mainly preferentially oriented columnar grains, the post-processing did not significantly alter the fatigue strength or fatigue crack growth threshold values. It was then concluded that SLM-processed parts may be used in applications without post-processing, except potentially turning to remove surface roughness.

LRM Inconel 625 was tested for fatigue crack growth and fracture toughness by Ganesh et al. [54]. 12 and 25 mm CT specimens were machined from bulk printed material with the crack growth parallel to the build growth direction. Tests were done with R values of 0.1 and 0.3 at 25 Hz in both  $K$ -increasing and  $K$ -decreasing modes. The Inconel 625 samples were characterized by steady crack growth (Paris' regime) in the  $\Delta K$  range of 14-38 MPa $\sqrt{m}$ , with FCGR results lower than wrought specimens. The integral fracture toughness values ( $J_{0.2}$ ) from CT were reported in the range of 196-255 kJ/m<sup>2</sup>. Ganesh et al. [43] reported that the fatigue crack growth of LRM 316L printed specimens was characterized by steady crack growth within the investigated  $\Delta K$  range of 11.4-24 MPa $\sqrt{m}$ , with FCGR results similar to that of annealed and 20% cold wrought worked.

$J_{0.2}$  values from CT were reported in the range of 147-259 kJ/m<sup>2</sup>, close to literature reported results of weld-metal 316L.

## 1.4 Research Objectives

With the growing desire to be able to additively manufacture industrial-grade parts, there is a clear need to explore how process parameters affect printed specimens. While there is a lot of research reported on SLM printed metals, most of it comes after process optimization and in the quasi-static range. It is, therefore, the purpose of this work to investigate the effects of different process parameters and print orientations on the high-strain rate mechanical behavior and defects on SLM printed stainless steel 316L.

Secondly, the printed specimens will be compared to wrought plate SS 316L. In order to accomplish this, ASTM standard mechanical test specimens were printed in two or three orientations using the two different process parameters. Mechanical properties were determined by performing both static and dynamic tests of varying types. Fracture surface and polished etched samples from each parameter and orientation sets were analyzed under optical and scanning electron microscopes. From these analyses it is expected that the second parameter parts will have better mechanical properties than the first set, and possibly comparable to wrought steel. It is also expected that the first parameter parts will be within range of wrought steel, even with an anticipated lower density.

## Chapter 2: Materials and Methods

### 2.1 Materials

The material used to print the specimens was Renishaw's vendor-supplied, gas atomized stainless steel 316L powder with a mean particle size of 30  $\mu\text{m}$  (with a range of 15-45  $\mu\text{m}$ ). Stainless steel 316L is a molybdenum (Mo) bearing austenitic steel known for its high mechanical strength and corrosion resistance [67]. The chemical composition range by percent weight of the powder given by the Renishaw safety data sheet is noted below in Table 3 [68].

Table 3: Renishaw Powder Chemical Composition [68]

<b>Chemical Name</b>	<b>Measured SS 316-L Composition (%w)</b>
Iron (Fe)	Balance
Chromium (Cr)	10-20%
Nickel (Ni)	1-10%
Silicon (Si)	1-10%
Copper (Cu)	0.5-1%
Manganese (Mn)	0.5-1%

#### 2.1.1 Powder Distribution Analysis

The powder size distribution analysis was performed on a Cilas 1190 laser particle size analyzer (Figure 15) located in Youngstown State University's (YSU) Geology Department. Approximately 1g of SS 316-L powder was inserted into the analysis

chamber to reach an obscuration value of 16%, which lies in the accepted range of 10-20%. The examination was done in the “wet” mode in which the analyzer utilizes three lasers to measure particles from 0.04-2,500  $\mu\text{m}$ . Fine particles are measured by the diffraction pattern, using either the Fraunhofer or Mie theory, whereas coarse particles are measured using a real-time Fast Fourier Transform of the image obtained with a CCD camera equipped with a digital processing unit (DSP) [69].

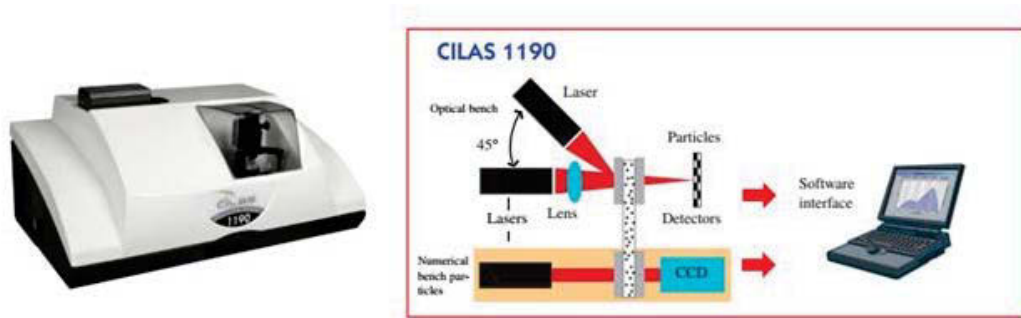


Figure 15: Cilas 1190 laser particle size analyzer and the schematic of how it determines particle sizes [69]

The powder was also examined under a JEOL JSM-7600F field emission (FE) scanning electron microscope (SEM) located in YSU’s Electron Microscopy Laboratory. This machine can do magnification up to 1,000,000x and has backscattering (BS), EDS, electron backscatter diffraction (EBSD), nanometer pattern generation system (NPGS), and scanning transmission electron microscopy (STEM) capabilities. 316L powder was attached to the SEM stage by means of carbon tape and imaged at multiple magnifications to show sizes, shapes, and distribution.

### 2.1.2 Powder Chemistry Analysis

The 316L powder supplied by Renishaw was examined using both X-ray fluorescence (XRF) and X-ray powder diffraction (XRD) at Youngstown State University's X-Ray Diffraction Lab. XRF analysis is done using EDS, which determines elemental composition, by mass, of elements heavier than neon (Ne) by shooting X-rays at the powdered sample and recording the detected energies of emitted photons resulting from the ejected electrons. The EDS used for the analysis, a S2 Ranger fluorescence spectrometer, uses a silicon-lithium [Si(Li)] detector and produces X-rays from a rhodium (Rh) and palladium (Pd) target, and the chamber is swept with helium (He) to garner the best results. The resulting composition is determined from detected wavelength peaks, which are labeled using shell identification (K, L, M) and transition ( $\alpha$  or  $\beta$ ), that are characteristic for each element. While XRF analysis can give a basic elemental composition, XRD analysis can identify the most likely compounds and crystallographic structures that make up the sample. A Bruker-Nonius D8 Advance Powder Diffractometer was used to examine the powder. It is equipped with a VÅNTEC-1 detector for fast simultaneous recording of X-ray diffraction patterns over a wide  $2\theta$  angular range.

## 2.2 Builds

In order to do this research, a Renishaw 250AM located at *America Makes* was used. It is fitted with a continuous wave Ytterbium fiber laser that runs in an inert atmosphere of argon (Ar) or nitrogen (N) to minimize oxidation of printed specimens, degradation of the powder [2], and providing efficient heat conduction and component cooling [70]. The

laser scans the powder bed using an f- $\theta$  lens and mirrors [33] following a predetermined scan strategy, a meandering strategy in this case. This means that the edges of the substrate may not get the same amount of laser energy as the middle because the lens does not move; instead the laser uses the movable mirrors to scan about the edges. The laser runs in a modulated operation pulsed with a TTL trigger [6], in which the laser hits a point, turns off, and moves a set distance away before melting the next point. This forms a static melt pool that is more stable than a dynamic one created by continuous laser scanning.

Once a layer has been scanned by the laser, the substrate and powder bed is lowered in the Z-axis one layer thickness by means of an elevator. Then the powder hopper dispenses a layer's amount of powder to be spread by the recoater. Due to the nature of the meandering scan strategy, each layer has its scan pattern rotated to avoid hitting the same points in subsequent layers to build a better part. A schematic of the build chamber [33] and machine specifications of the Renishaw 250AM [7, 71, 72] can be seen below in Figure 16 and Table 4, respectively.

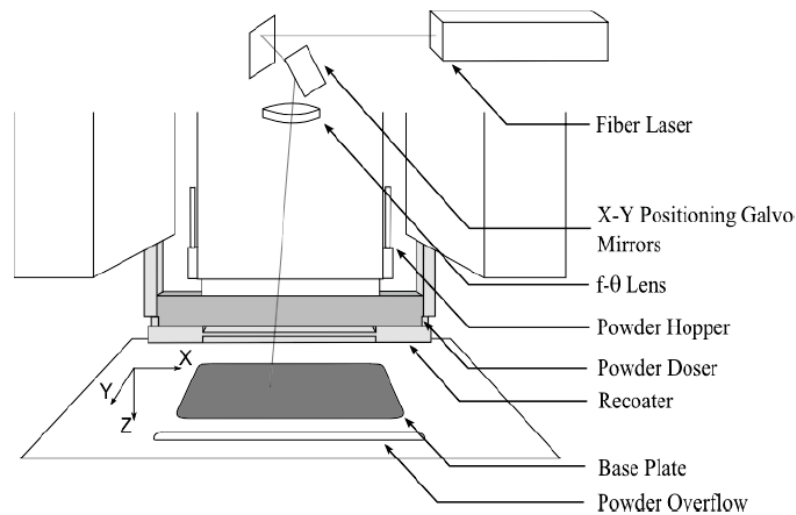


Figure 16: Renishaw AM 250 Internal Diagram [33]

Table 4: Renishaw AM250 Specifications [7, 71, 72]

<b>Build Volume (mm)</b>	245 x 245 x 300 (X, Y, Z)
<b>Laser Power (W)</b>	200
<b>Laser Beam Diameter (<math>\mu\text{m}</math>)</b>	70 at powder surface
<b>Maximum Scanning Speed (mm/s)</b>	2000
<b>Build Rate (<math>\text{cm}^3/\text{hr}</math>)</b>	5 – 20
<b>Layer Thickness (<math>\mu\text{m}</math>)</b>	20 – 100
<b>Part Tolerance</b>	$\pm 0.05$
<b>Material Waste</b>	95% of material reusable after sieving

In an effort to determine the effects of defects on the printed samples, there were two sets of process parameters used: those originally in the printer (Set 1) and Renishaw’s standard (Set 2), which are shown in Table 5. Between the two sets of parameters, laser scan speed, exposure time, and point difference was changed, while



laser power was not changed. From these parameters the laser energy densities are 54.59 for set 1 and 58.06 for set 2, according to Equation (3).

Table 5: Two Sets of Printer Process Parameters

<b>Parameter Set</b>	<b>Laser Power</b> <i>P</i> (W)	<b>Scanning Speed</b> <i>v</i> (mm/s)	<b>Exposure Time</b> <i>t</i> (μs)	<b>Point Difference</b> <i>d</i> (μm)
1	200	590	110	65
2	200	550	90	50

The *XY*-orientated specimens were printed horizontally on the build plate, *ZX*-orientated specimens vertically, and *XZ*-orientated specimens on edge as shown below in Figure 17. These specimen groups are labeled according to ASTM F2921 [4] in which the orientation is described by listing the axes of the AM machine that are parallel to the first and second longest dimensions. This is explored to determine if part orientation has any effect on the mechanical properties or possible inherent defects. Parts, with or

without supports, were removed from the substrate using a band saw at *M7 Technologies* and, if needed, machined to ASTM standards.

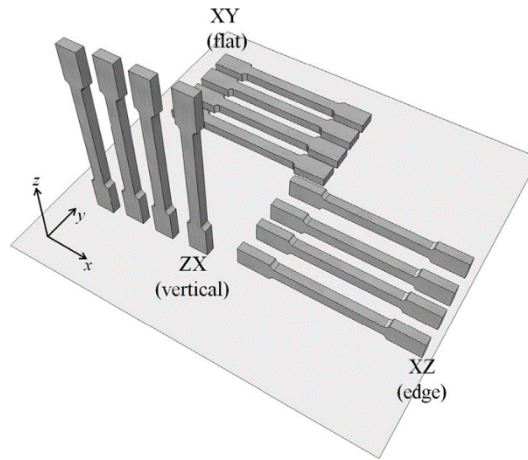


Figure 17: Orientation of the three orthogonal specimen orientations labelled according to ASTM F2921 [13]

## 2.3 Microstructural Analysis

Samples were printed in the *XY* and *ZX* orientations for each set of process parameters and then prepared for microstructural examinations. The prepared samples were investigated using both an optical microscope (OM) and scanning electron microscopes (SEM) prior and after being chemically etched.

### 2.3.1 Preparation of Samples

Samples were taken from bulk printed material. Cross-sections of parts printed in the *XY* (flat) and *ZX* (vertical) orientations were cut using a Buehler IsoMet 1000 precision saw and set into epoxy to be properly prepared for imaging. The properly set samples were then ground and polished on a Planopol-2 polishing table using a variety of silicon-carbide (SiC) abrasive papers and alumina polishing suspension. Grinding started with

220 grit to attain a flat surface before using 320, 800, 1000, 2400, and 4000 grit papers while rotating samples 90° each time to remove scratches while nearing a mirror finish. When a suitable, flat surface was achieved, the samples were polished using 9 μm, 3 μm, and 1 μm polishing cloths with an alumina suspension.

### 2.3.2 Polished Surface Analysis

Sections that were cut, set in epoxy, and polished were first examined under a Zeiss-Axiophot light microscope with an attached Pixielink-model PL A662 CCD camera. Images were taken at a total magnification of 100x (10x objective and 10x eyepiece). Those images were then processed using ImageJ software for initial porosity measurements. This software transforms the typical image format (TIFF in this case) by splitting it into channels (red, green, blue) in which a threshold can be selected to choose the porous areas to be analyzed [73].

The samples were chemically etched using Kalling's 2 Reagent, or Kalling's waterless reagent, (100 mL concentrated hydrochloric acid, 5 g cupric chloride, 100 mL ethyl alcohol), which develops dendritic patterns in steel and attacks ferritic (darkened) and martensitic (darker) [74]. Samples were immersed for two minutes each and cleansed, and the etching for grain structure was confirmed underneath a light microscope (LM). The samples were then studied in the JEOL JSM-IT300LV variable pressure (VP) SEM for microstructure and grain structure.

A second round of polished samples were etched with Vilella's reagent (1 g picric acid, 5 mL hydrochloric acid, 100 mL ethyl alcohol), which delineates austenite grain

boundaries in a martensite steel [74]. This was used in an attempt to examine grain boundaries and melt pool networks using an optical microscope.

### 2.3.3 Fracture Surface Analysis

Fracture surfaces were taken from the specimens with median results for each orientation of tensile and Charpy V-notch impact tests using the precision saw. The fracture surfaces were sonicated in isopropyl alcohol for cleansing and then mounted on the stage using carbon tape. The surfaces were examined in the FE SEM and cracks were investigated and characterized in low and high magnification mode. It was attempted to determine what effect orientation and process parameters had on the fracturing of the specimens. Possible contaminants were investigated using the low-angle backscattered electron (LAGE) backscatter detector to determine elemental composition using the built-in EDS. The SEM used an Energy Dispersive Analysis X-Ray (EDAX) detector to determine different elemental spectra peaks to determine composition of areas.

## 2.4 Mechanical Testing

### 2.4.1 Hardness Testing

Two different standard hardness tests were performed in the Strength of Materials lab in the Civil and Environmental Engineering department at YSU. First, a printed 0.25-inch-thick plate from each process parameter set was printed in the ZX orientation and ground to a flat finish. Then, each plate's hardness was tested using the Rockwell D and Brinell

methods. By using two different methods and comparing results, a better understanding of the results was expected, both mechanically and materialistically.

The Rockwell D test was the first performed following ASTM E18-15 [75] and was done on a Buehler Macromet 3 hardness tester. Each plate was indented five times in a straight line through the middle portion with a diamond tip at a 100 kg major load, intrinsic features of the D Rockwell scale. Next, Brinell testing was done following ASTM E10-15a [76]. The test used a Tinius Olsen Air-O-Brinell testing apparatus fitted with a 10 mm tungsten carbide spherical indenter at a load of 3000 kg for 20 seconds. Four separate indentations, at a proper distance away from previous ones, were done on each plate and then indentation diameters were measured. These measured diameters were converted into Brinell hardness number (*HB*) using an approximate hardness relations chart for steels. The Rockwell D hardness number (*HRD*) and *HB* were compared to each other as well as to reported wrought values. It was also hoped to be able to determine some intrinsic material properties from the hardness results.

#### 2.4.2 Quasi-Static Tensile Testing

Flat, dog-bone tensile bars were designed in SolidWorks according to the standard subsize dimensions per ASTM E8/8M [51] and E370 [60], as seen below in Figure 18 and Table 6. The bars were then printed in the *XY* (flat) and *ZX* (vertical) orientations for the first set of parameters, and in the *XY*, *ZX*, and *XZ* (edge) orientations for the second set, as seen in Figure 17 [13]. The first batch of parts were printed directly onto the substrate with a 3 mm allowance for band saw removal. The second batch used 2.5 mm tall supports. In addition to testing additively manufactured bars, flat bars were machined

from 0.25-inch-thick stainless steel 316L wrought plate, also according to the ASTM E8/8M subsize standard.

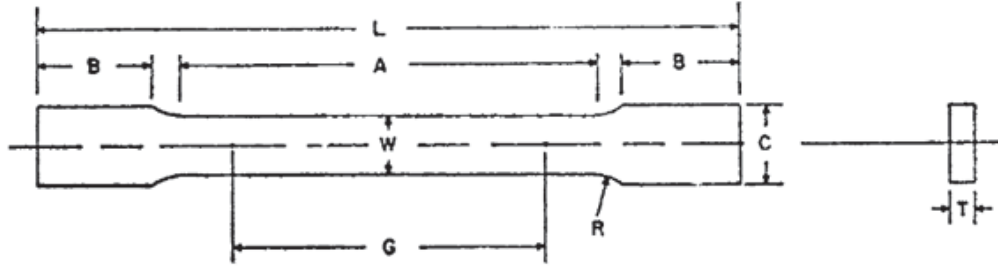


Figure 18: ASTM E8/8M-09 rectangular tension test specimen schematic [51]

Table 6: ASTM E8/8M metric subsize standard for rectangular flat-bar tensile test specimen dimensions [51]

	<b>ASTM Standard (6 mm Wide)</b>
Gage length (G)	$25.0 \pm 0.1$
Width (W)	$6.0 \pm 0.1$
Thickness, max (T)	6
Radius of fillet, min (R)	6
Overall length, min (L)	100
Length of reduced section, min (A)	32
Length of grip section, min (B)	32
Width of grip section, approximate (C)	10

Before being tested, each bar was wiped down with alcohol swabs to remove any contaminants. Then an Omega precision strain gage, specifications shown in Table 7, was super-glued to the middle of the gage length on each side. Prior to every individual test, each strain gage lead was soldered to a lead wire from a P3 strain indicator and recorder. The lead wires were connected to the strain indicator using half-bridge circuits.

Table 7: Omega Precision Strain Gage Characteristics

<b>Strain Gage Code</b>	SGD-6/120-LY11
<b>G.F. Value</b>	2.13
<b>Resistance</b>	120 Ohms
<b>Tolerance</b>	+/- 0.35%

Quasi-static tensile testing occurred on an Instron 4206 universal testing machine with a 150 kN load cell set in an Instron 5500R mounting. In order to control, record, and export necessary data, Instron's Bluehill 3 software was used. A method was created to record the load and displacement of the crosshead using a strain rate of 0.47625 mm/mm/min. The strain rate was determined using the qualification that the maximum crosshead rate should be  $0.015 \times A$  mm/mm/min where 'A' is the length of the reduced cross-section of the specimen [77]. Even though the thickness of the gage lengths were different between the additively and traditionally manufactured specimens, their lengths were all 32 mm.

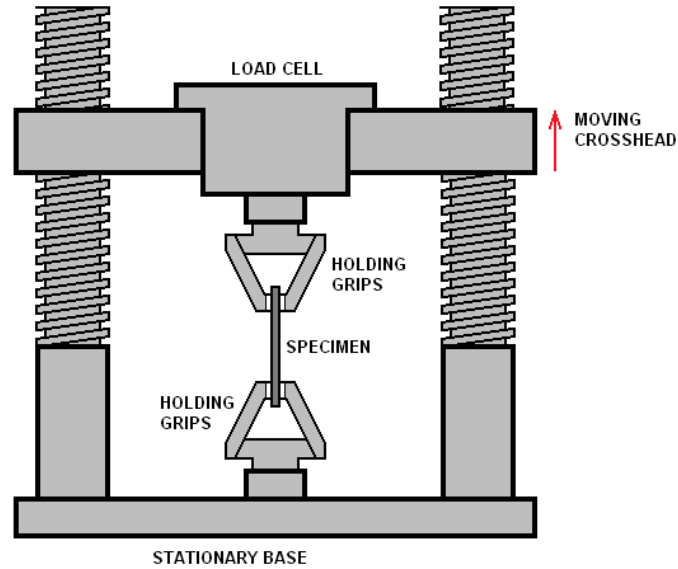


Figure 19: Tensile test schematic [78]

### 2.4.3 Split-Hopkinson Compression Testing

High strain-rate compression testing was done using an REL SHPB setup with specimens printed in the XY and ZX orientations. Dimensions of the cylindrical specimens were a length of 9.1 mm and diameter of 8.8 mm, printed with supports. The SHPB had a 152.4 mm long, 19.05 mm diameter striker bar of stainless steel that was launched by a gas gun of 100 psi. Waves were recorded using strain gages on the incident and transmission bars as the specimen was sandwiched between them (Figure 20). The experimental setup was controlled using the software PicoScope.



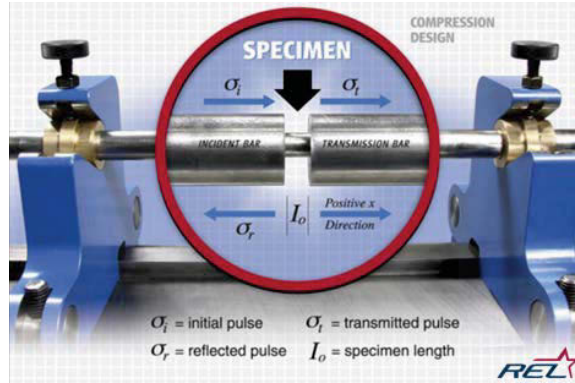


Figure 20: Specimen setup between incident and transmission bars of SHPB [79]

The resulting signals were collected by the signal conditioning amplifier and analyzed using the software SURE-Pulse (Figure 21). This software uses inputs such as sample dimensions, density, and quasi-static Young's modulus (from tensile testing), as well as striker bar dimensions and density to create stress and strain values. The high-strain rate elastic modulus, yield point, and ultimate strength can be determined from the exported data points or from the software created stress-strain curve.

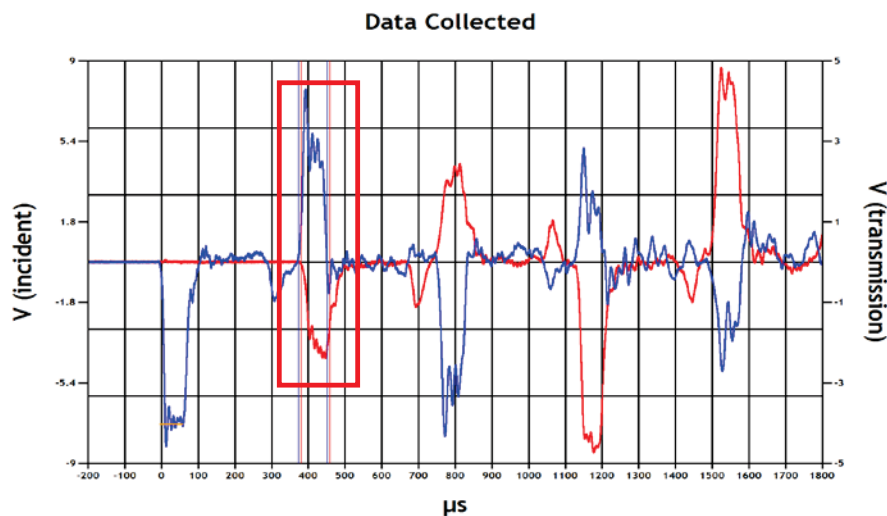


Figure 21: Typical wave response capture in SURE-Pulse from specimen 3 from the ZX-2 group. The point of the first simultaneous incident/transmitted wave signal is chosen for analysis.

#### 2.4.4 Charpy V-Notch Impact Testing

Charpy V-notch specimens were machined from rectangular blocks printed in the *XY* and *ZX* orientations. The rectangles were designed in agreement with ASTM E370 [60] at the standard size of 10 mm x 10 mm x 55 mm (Figure 22), and then 0.25 mm notches were machined at 45° using an electrical discharge machine (EDM) by *Bancroft Farms*. The *XY* and *ZX* specimens had the notch machined on the side parallel to the build layers, while the *XZ* specimens had the notch machined on the top surface perpendicular to the build layers (Figure 23).

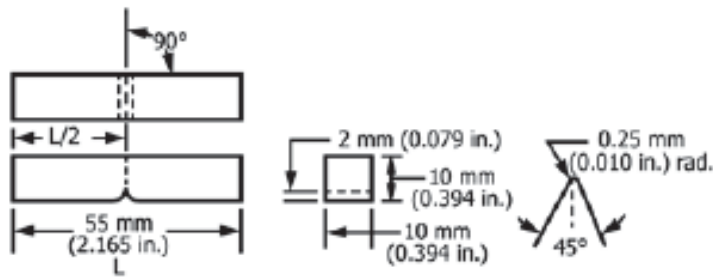


Figure 22: ASTM E370 standard dimensions for Charpy V-notch specimens [60]

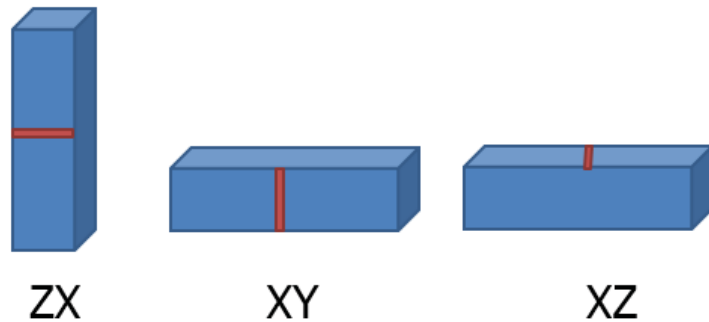


Figure 23: Notch orientations for each specimen group

The specimens were set into the holder on the Charpy impact mechanism with the notch facing away from the impacting hammer, following ASTM 23-12c [80]. A Tinius Olsen model IT 406, located in the YSU Civil Engineering lab, was used for testing by means of a fifty pound hammer that was latched at six feet off of the ground. This was such that it delivered 300 foot-pounds of energy for specimen impact fracturing. The machine was calibrated and then utilized a computer to record the impact resistance for each specimen, as shown in Figure 24.

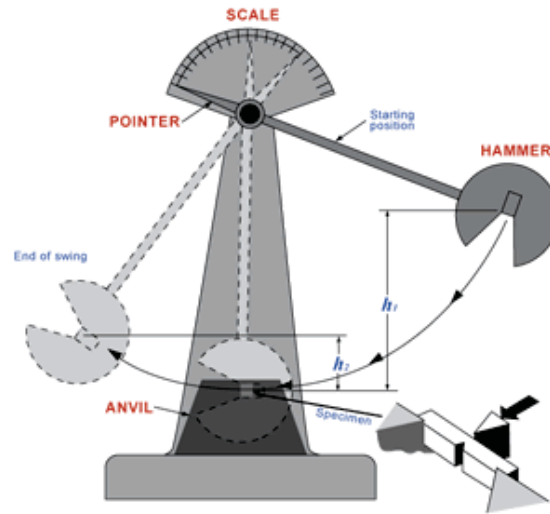


Figure 24: Schematic of Charpy V-Notch mechanism [81]

## Chapter 3: Results and Discussion

### 3.1 Powder Analysis

#### 3.1.1 Powder Sizing and Distribution

Results of the tested sample show that the material had a distribution ranging between approximately 10  $\mu\text{m}$  and 50  $\mu\text{m}$ . The distribution and volume undersize plot can be seen below in Figure 25.

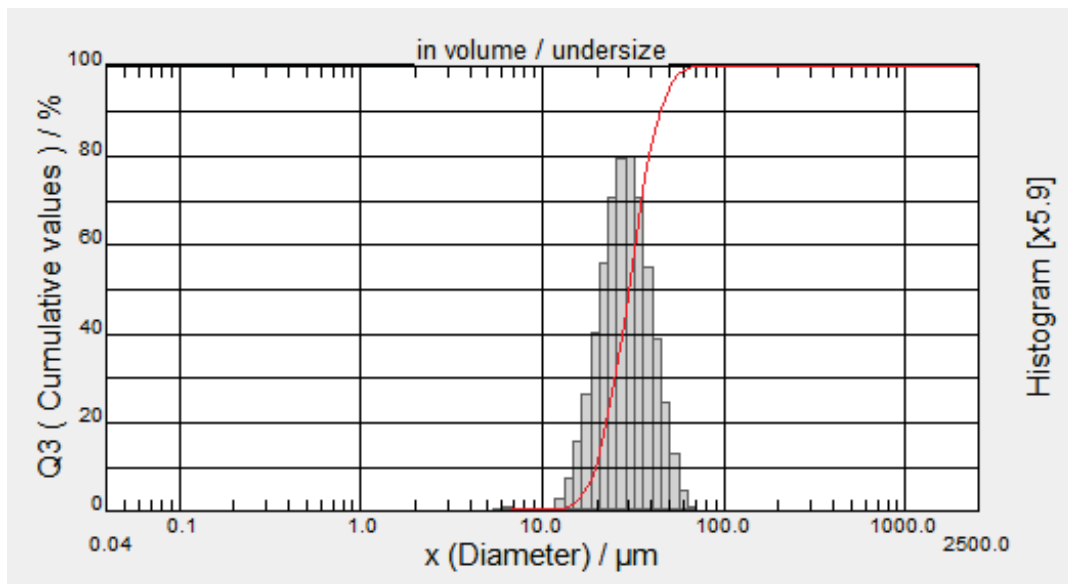


Figure 25: Particle size distribution measured using Cilas 1190 in liquid mode

The 10<sup>th</sup>, 50<sup>th</sup>, and 90<sup>th</sup> percentiles for the size were then determined and found to be approximately 19.51  $\mu\text{m}$ , 29.84  $\mu\text{m}$ , and 44.67  $\mu\text{m}$ , respectively. Therefore, even though it was found that there were particles that were outside of the 15+/-45 Renishaw powder size range, the powder distribution between the 10<sup>th</sup> and 90<sup>th</sup> percentiles were within range.

The powder was also examined using a JEOL JSM-7600F variable pressure SEM at YSU's Materials Characterization Laboratory. SEM images of the 316L powder at magnifications of 150x, 500x, and 1800x are shown in Figure 26. While the powder appears to be mostly spherical, oblong and agglomerated particles can be seen across the distribution.

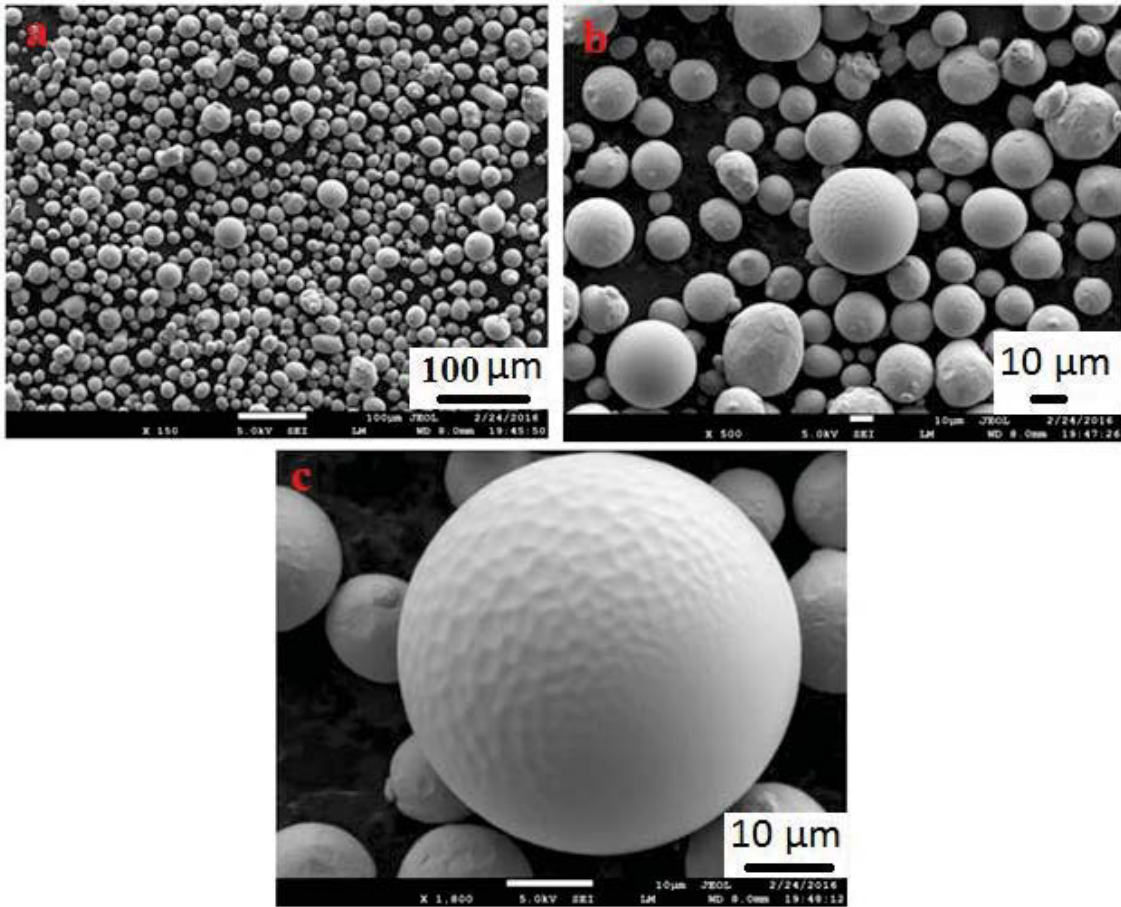


Figure 26: Secondary backscatter images of powder at 150x magnification (a), 500x magnification (b), and 1800x magnification (c)

### 3.1.2 Powder Chemistry

Results from the XRF examination of the 316L powder are presented in Table 8 and compared to the ASTM A240 standard. The inability of the XRF to measure elements

lighter than Na expected in 316L, such as N and C, may have skewed the results.

However, the chemical composition matches all of the other criteria of ASTM A240 [82].

Table 8: XRF Chemical Composition by Weight Percentage of SS 316-L Powder

<b>Chemical Name</b>	<b>ASTM A240 SS 316 L Composition (%w) [82]</b>	<b>Measured SS 316-L Composition (%w)</b>
Iron (Fe)	Balance	Balance
Chromium (Cr)	16.0-18.0	17.898
Nickel (Ni)	10.0-14.0	10.330
Silicon (Si)	0.75 Max	0.499
Manganese (Mn)	2.00 Max	1.363
Molybdenum (Mo)	2.00-3.00	2.220
Phosphorus (P)	0.045 Max	0.017
Nitrogen (N)	0.10 Max	-
Carbon (C)	0.03 Max	-
Sulfur (S)	0.03 Max	-
Copper (Cu)	-	0.133
Vanadium (V)	-	0.024
Niobium (Nb)	-	0.007

A Bruker-Nonius D8 Advance powder diffractometer was used for the XRD and the analysis determined a cubic, face-centered (Fm-3m) crystal structure with a unit cell length of approximately 3.618 angstroms (Å). The resulting spectrums from the XRF and XRD work are attached in the appendix.

### 3.2 Microstructural Analysis

Samples from each parameter set and print orientation were cut using a precision saw and set into epoxy before being ground and polished. After proper preparation, the samples were chemically etched for two minutes using Kalling's 2 reagent before being examined under an optical microscope and variable pressure scanning electron microscope. The etchant is known for darkening martensite and attacking ferrite while only slightly attacking austenite. Since the etchant attacks steel structures, analysis is on what structures can be identified in the SLM printed 316L and any differences between print orientations. A second set of polished samples were etched for 40 minutes in Vilella's reagent, an etchant known to dealienate austenite in a martensitic steel. These samples were examined in low magnification under a optical microscope. Any print defects were also investigated, as well as surface porosity and microporosity.

In the specimens from the first set of process parameters, a higher level of porosity is seen across the polished surfaces. At the lower magnification of the optical microscope (10x in the eyepiece and 5x or 10x of the optical lens), larger defects can be seen as well as darker regions assumed to be some structure other than the regularly seen austenite in 316L. However, deeper scratches can also be seen as a result of the grinding and polishing process, and some surface contamination can also be seen. At the slightly

higher magnification of the VP SEM (150x), a few pores and micropores can be seen, and there also appear to be some other structures in the images. The differences between the orientations are not excessive, but there is some contrast in the micrographs that can explain mechanical anisotropy. In the *XY* orientation, Figure 27, there are more darkened areas than in the *ZX* orientation, Figure 28, which points towards more microstructural variance. The addition of structures such as bainite or martensite could add hardness and yield and ultimate strength properties to the SLM parts. These structures could be from the rapid heating and cooling [76] that occurs in the SLM process.

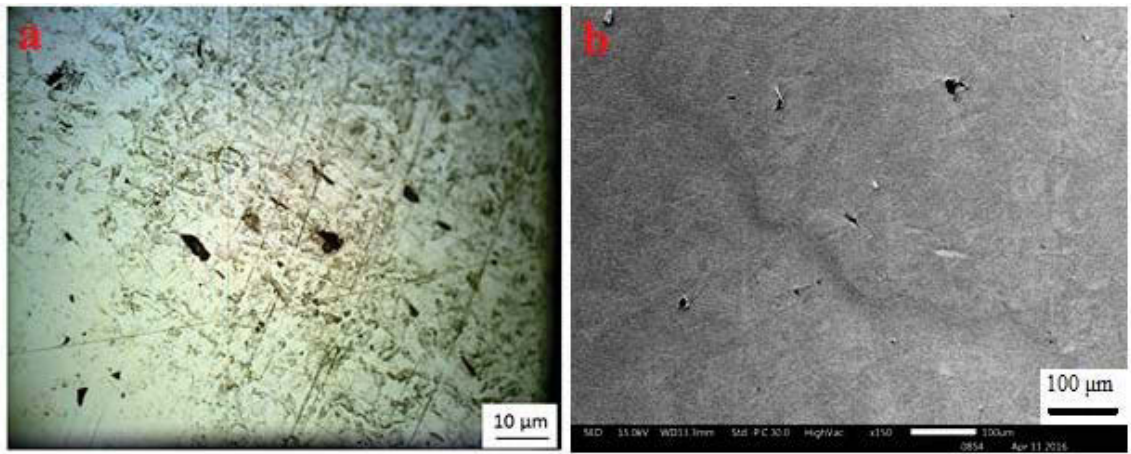


Figure 27: (a) Parameter 1 *XY* orientation polished sample examined under 100x light microscope and (b) 150x secondary electron micrograph of the same sample.



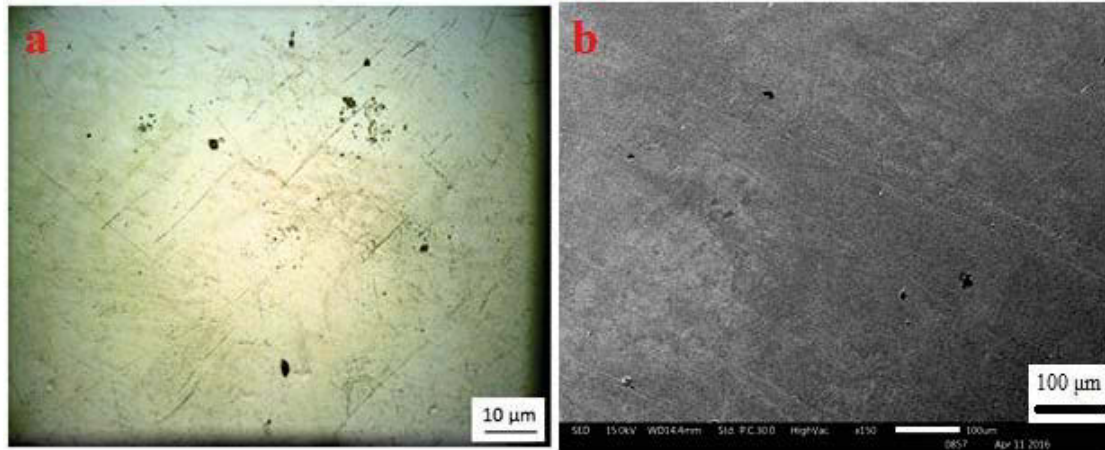


Figure 28: (a) Parameter 1 ZX orientation polished sample examined under 100x optical and (b) 150x secondary electron micrograph of the same sample.

While the *XY* orientation of the second parameter set, Figure 29, appears to have a similar amount of pores and micropores, the surface of the *ZX* orientation in Figure 30 appears denser. In the optical micrographs, Figures 29a and 30a, more contrast is seen and once again assumed to be varying steel structures, though in larger amounts. This could be due to decreased exposure time and point difference, which increases the melt pool overlap and the solidification rates of the material. Such an increase in melting and cooling rates could increase the formation of those other steel constituents. Of interest in these micrographs is the presence of metallic balling in the *XY* orientation. This occurs when the molten material is viscous or at a high wetting angle so that agglomerates or metal particles cluster on the surface or, in this case, a pore. Metal particles are easily seen in the in the pore in the VP SEM image at 150x magnification. The lack of fusion defect is also more easily seen as two molten areas do not quite overlap, leaving a sizable porous defect. Other than this large defect, a few other small pores in the *XY* orientation and a medium-sized pore in the *ZX* orientation, there are fewer overall defects in the

micrographs, leading to the assumption that the second set of parameters manufactured parts that contain higher densities than the first process parameters. Also of interest in the ZX orientation is possible grain structures in the bottom left corner appearing in the range of 25-100  $\mu\text{m}$ . It should be noted that not all of the pock marks in these images, especially in the optical micrographs, are pores, but instead, are most likely pitting due to excessive chemical etching.

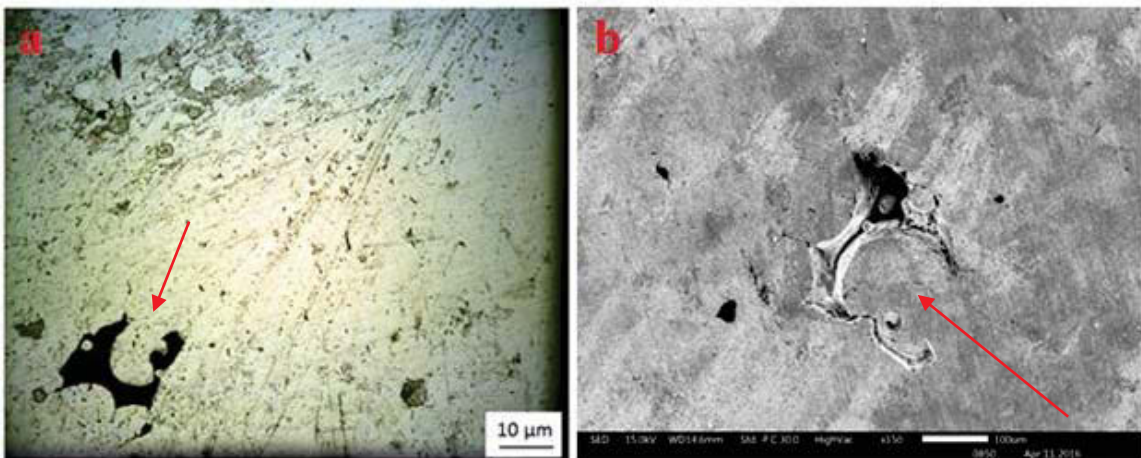


Figure 29: (a) Parameter 2 XY orientation polished sample examined under 100x optical and (b) 150x secondary electron micrograph of the same sample.

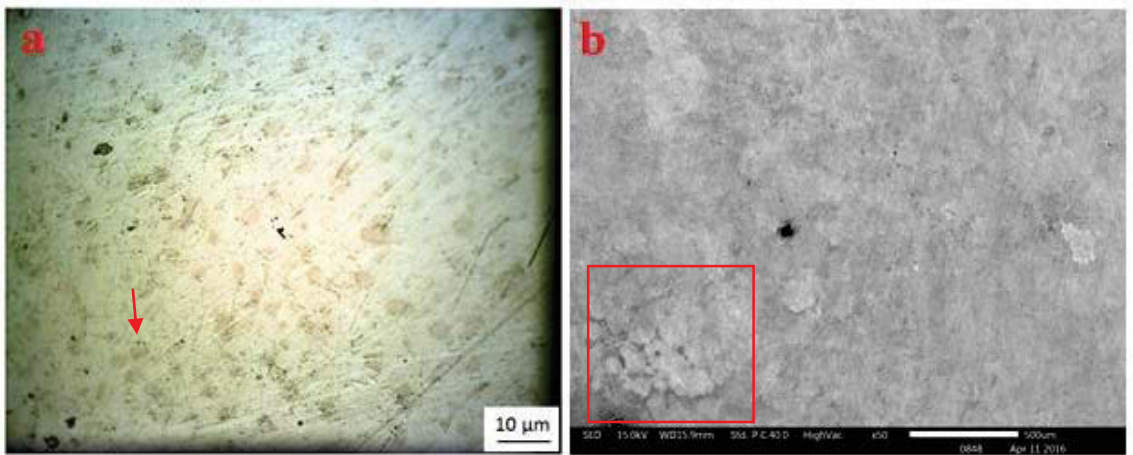


Figure 30: (a) Parameter 2 ZX orientation polished sample examined under 100x optical and (b) 50x secondary electron micrograph of the same sample.

Etching samples of the *XY* orientation of both parameter sets with Vilella's reagent highlighted the microstructure of the SLM printed 316L. In Figure 31, the microstructure of the two process parameter sets is emphasized. The melt pool networks and grain structures are shown with the second parameter set showcasing a smaller grain size, which means a higher strength. In both micrographs there are clear instances of porosity and lack of fusion defects, especially in the bottom right corner of (a). However, once again the second set of parameter specimens are seen to have less porosity.

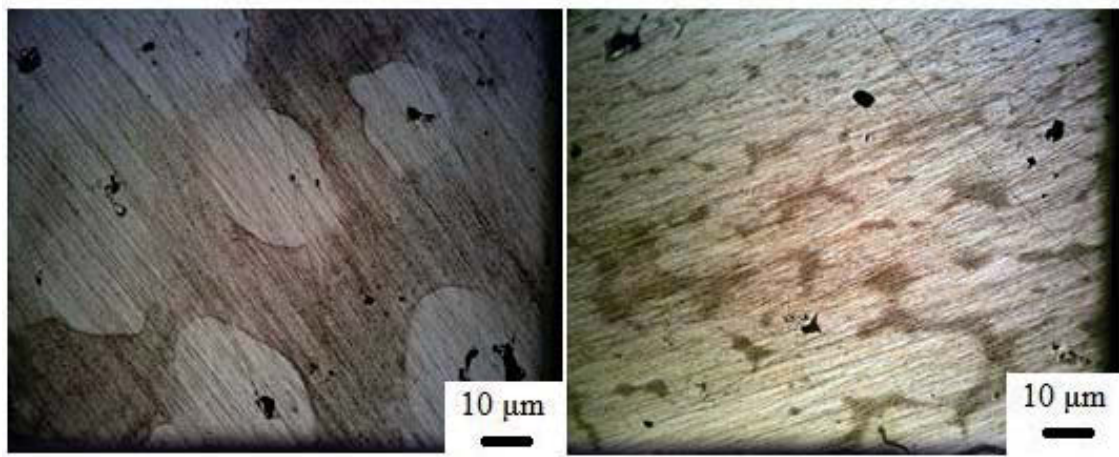


Figure 31: (a) 50x optical micrographs of parameter set 1 and (b) set 2 showcasing the SLM microstructure

Due to the microstructure and mechanical properties realized in the SLM printed 316L, a more thorough investigation of the structures was done. A continuous cooling transformation (CCT) diagram was used to hypothesize about the possibility of a structure increasing the strengths such as bainite or martensite. The rapid solidification and cooling that occurs in the SLM process can lead to structure transformation, and using the diagram in Figure 32 it can be guessed that there was austenite transforming into martensite.

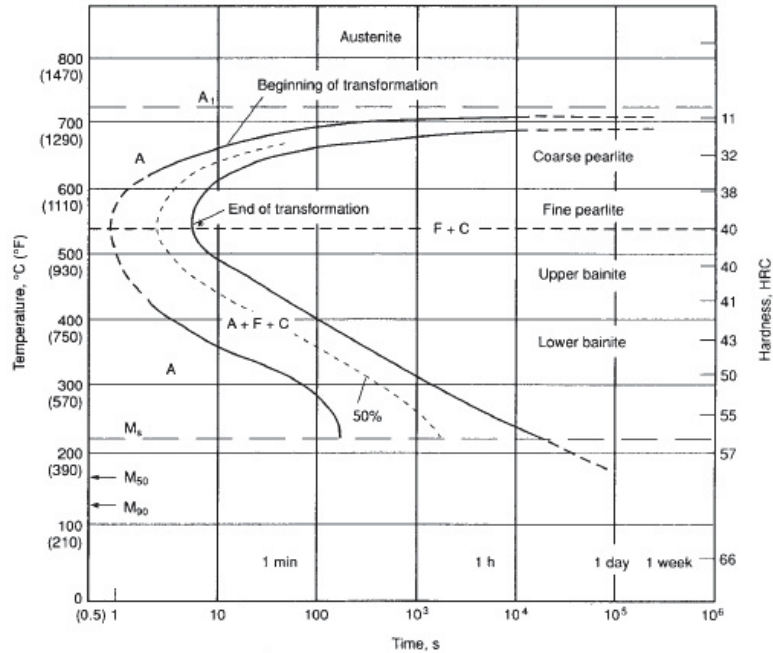


Figure 32: Continuous cooling transformation (CCT) diagram of a low carbon steel showing the different structures possible at different cooling rates [83]

Using the software ImageJ, a basic density analysis was performed because the Archimedes analysis was not conclusive. Optical images were taken from the polished specimens and then analyzed using the contrast to get a rough estimate of the porosity of the different parameter sets and orientations, as shown in Table 9. In both orientations it was determined that the second set of process parameters improved the density. It must be noted, however, that this method only gives a rough estimate and not precise porosity results because the porosity is chosen from the contrast of the images at the user's discretion.

Table 9: Porosity results using ImageJ software and optical micrographs at 100x

<b>Sample</b>	<b>Porosity (%)</b>
<i>XY-1</i>	9.46 ± 2.1
<i>XY-2</i>	8.62 ± 2.8
<i>ZX-1</i>	7.69 ± 3.7
<i>ZX-2</i>	3.75 ± 2.2

### 3.3 Mechanical Testing

#### 3.3.1 Hardness Testing

Quarter-inch thick plates printed in the *ZX* orientation were manufactured using both sets of process parameters and had their hardness tested using both the Rockwell and Brinell methods. The Rockwell tests were performed on a Buehler Macromet 3 apparatus fitted with a Brale indenter and major load of 100 kg, so that they fit the requirements of a Rockwell D. The Brinell tests were performed on a Tinius Olsen Air-O-Brinell apparatus fitted with a 10 mm tungsten carbide spherical indenter and a major load of 3000 kg. The averaged results and converted equivalent tensile strengths were then compared to reported wrought 316L results, as shown in Table 10.

Table 10: Brinell and Rockwell D test results on SLM printed 316L with two different process parameter sets and compared to reported wrought results.

Process Parameter	Brinell (HB)	Rockwell (HRD)	Equivalent Tensile (MPa)
1	150.6 ± 7.4	26.6 ± 0.9	521
2	180.4 ± 7.1	30.7 ± 0.9	558-612
<i>WP</i>	170	33	579

It is not surprising that the second process parameter plate outperformed the first set of parameters due to the decrease in porosity, although for that same reason it is surprising that it compares so favorably to the wrought plate, which has an even higher density. While density does play a major roll, as well as surface roughness, in hardness testing, the microstructure and composition also influence the hardness numbers quite a bit. As can be seen in literature, different structures found in steels have varying hardness values and can severely influence the material as a whole. Therefore, adding these hardness values with the micrographs, an increase in martensite can be assumed in the second set of process parameter parts.

While other studies have mainly employed Vickers hardness tests, using the relations table can give a decent comparison. Tolosa et al. [37] reported an average of 235 HV, which is equivalent to about 229 HB or 40.5 HRD, while Cherry et al. [10] reported a similar average value of 225 HV, corresponding to about 220 HB or 39.5 HRD. Cherry et al. noticed an increase in hardness with a decrease in porosity. They also determined that point distance had a greater effect on surface roughness than did

exposure time, which could help explain the better results seen in the second parameters since smaller point distance equates to better surface quality.

### 3.3.2 Quasi-Static Tensile Testing

Tensile tests were performed on an Instron 4206 universal testing machine with a constant strain rate of 0.47625 mm/mm/min. Five tensile specimens were printed using the first set of process parameters in the ZX and XY orientations to determine anisotropy and mechanical strength. The median stress versus strain plots for the two printed orientations using the first set of process parameters and wrought 316L plate are shown below in Figure 32 to represent the entire group of specimens using the strain gages.

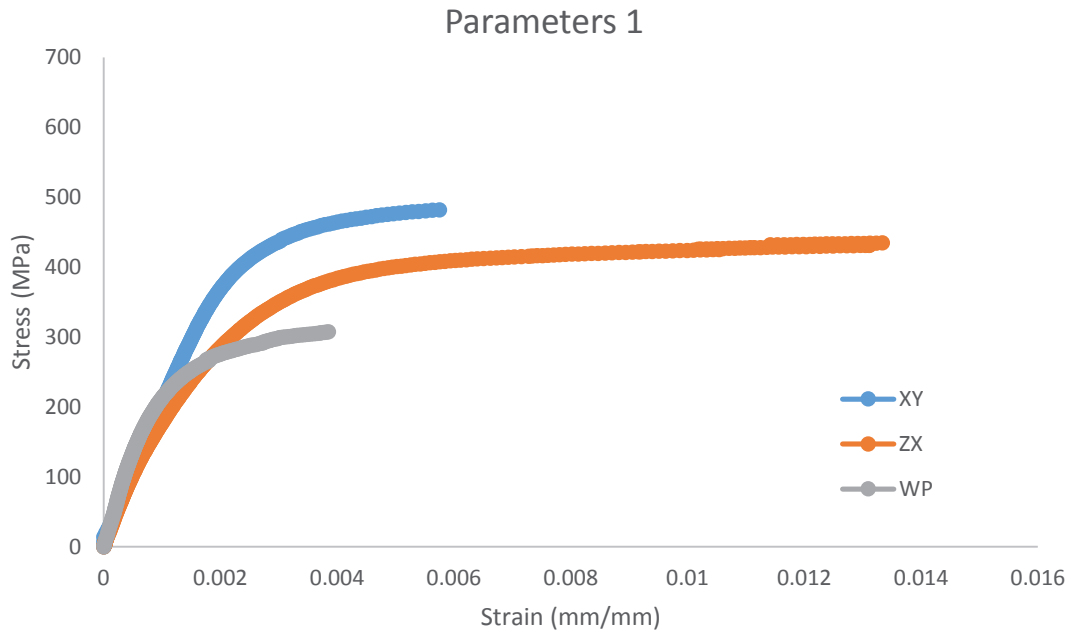


Figure 33: Stress-strain curves of the first set of parameters and wrought plate components using strain gages and strain indicator

In Figure 33 is the stress-strain curves using the crosshead extension of the Instron and gauge lengths of the specimens to showcase the specimen ductility in percent strain. It was from the Instron crosshead extension stress-strain curves that the ultimate tensile and 0.2% yield strengths were determined.

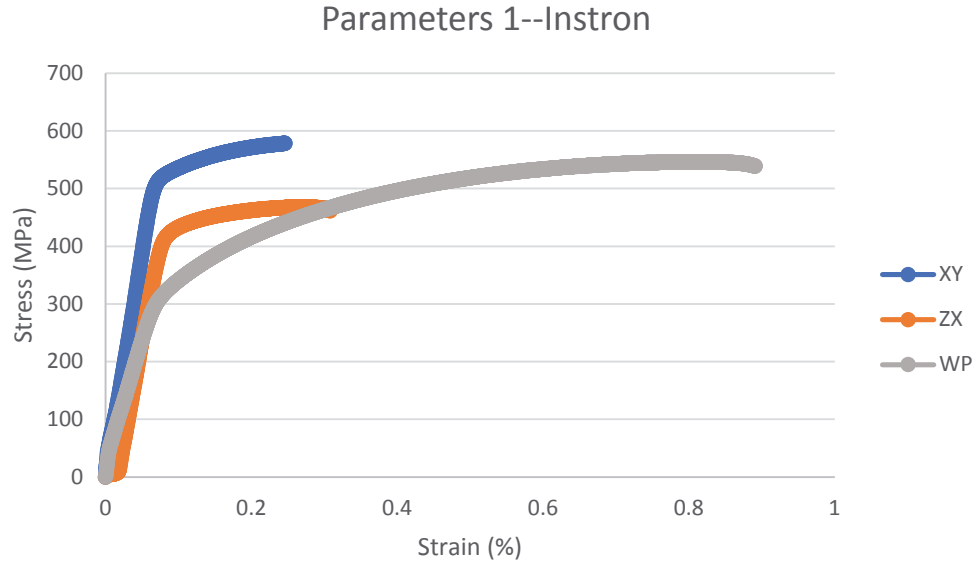


Figure 34: Stress-strain curves of the first set of parameters and wrought plate components using the Instron crosshead extension for yield and ductility

From the stress-strain curve of each individual trial and the exported data, tensile properties such as Young's modulus, ultimate tensile strength, and 0.2% yield strength were determined. The reduction of area was measured from both fracture surface of each sample and then averaged. The average results, along with the average standard deviation, is shown below in Table 11 and are compared to data from the Senvol database for Renishaw 316L [84].



Table 11: Tensile Properties of Parameter Group 1 and Wrought Plate Samples

<b>Specimen Group</b>	<b>E (GPa)</b>	<b>UTS (MPa)</b>	<b><math>\sigma_y</math> (MPa)</b>	<b>Reduction of Area (%)</b>
<i>XY</i>	185 ± 39	584 ± 12	486 ± 13	27 ± 9
<i>ZX</i>	153 ± 71	441 ± 81	365 ± 79	46 ± 6
<i>WP</i>	191 ± 22	585 ± 57	260 ± 59	67 ± 2
<i>Senvol Results [84]</i>	150-195	585-686	-	45-59
<i>Senvol Post-Processed Results [84]</i>	147-194	575-615	-	56-74

The first set of printing parameters were not able to meet the wrought specimens in reduction of area, but the flat-printed tensile bars are within range of the wrought specimens tested in terms of ultimate strength and elastic modulus. The vertically-printed tensile specimens do not have ultimate strengths or elastic moduli within range of wrought 316L. However, both printed orientations have much higher yield strengths than the wrought. When compared to the information from the Senvol database, however, the tensile results are within the range of the elasticity, though the other properties only fit depending on the build orientation.

The tensile results are easier to comprehend after examining the fracture surfaces in the FE SEM. The wrought plate, Figure 34c, fractured under ductile conditions proved by dimples and craters. This behavior is also seen in the *XY* (a) and *ZX* (b) orientations, though with much larger dimples than the wrought plate. There are also more defined ridges in the AM samples and cracks stemming from the larger dimples. The weaker *ZX*

tensile samples could be due to areas of brittle fracture shown by shelf-like structures in the bottom of 34b.

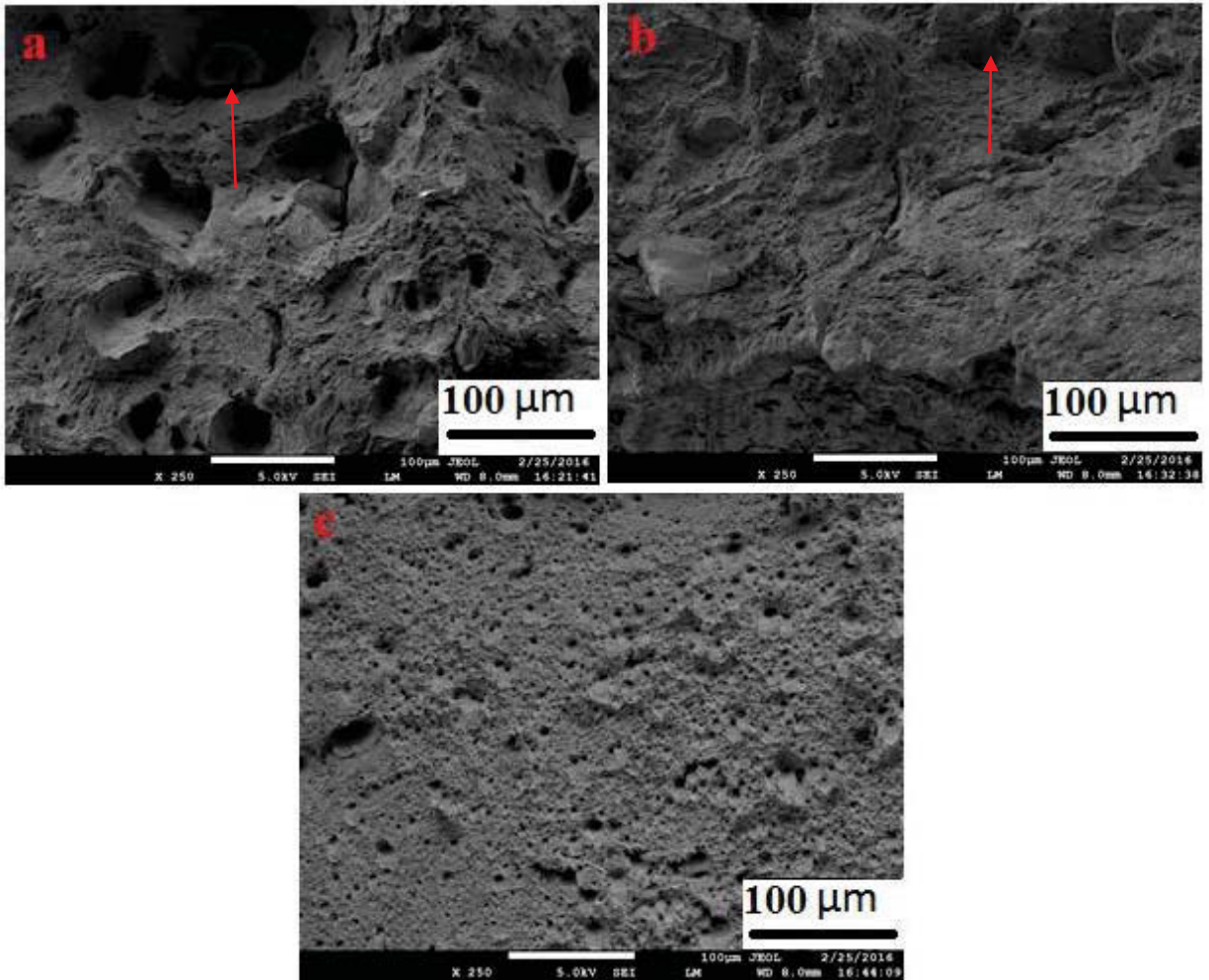


Figure 35: (a) Secondary electron micrograph from the parameter 1 tensile fracture surface images at 250x: *XY* orientation, (b) *ZX* orientation, (c) and wrought plate.

Using the second set of process parameters, five specimens were printed in the *XY*, *ZX*, and *XZ* orientations to compare to the first round of specimens and wrought plate. The median stress-strain curves for the second set of printer parameters can be seen below in Figure 35.

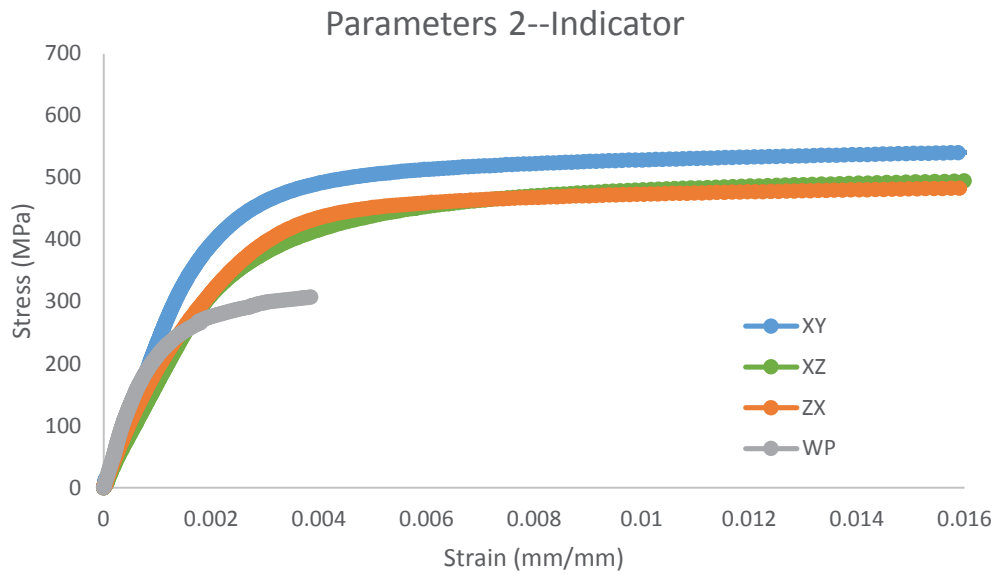


Figure 36: Stress-strain curves of the second set of parameters and wrought plate components using strain gages and indicator

In Figure 36 is the stress-strain curve using the crosshead extension to again showcase the ductility values in percent strain. Once again it was from the Instron-based curves that the ultimate tensile and 0.2% yield strengths were determined.

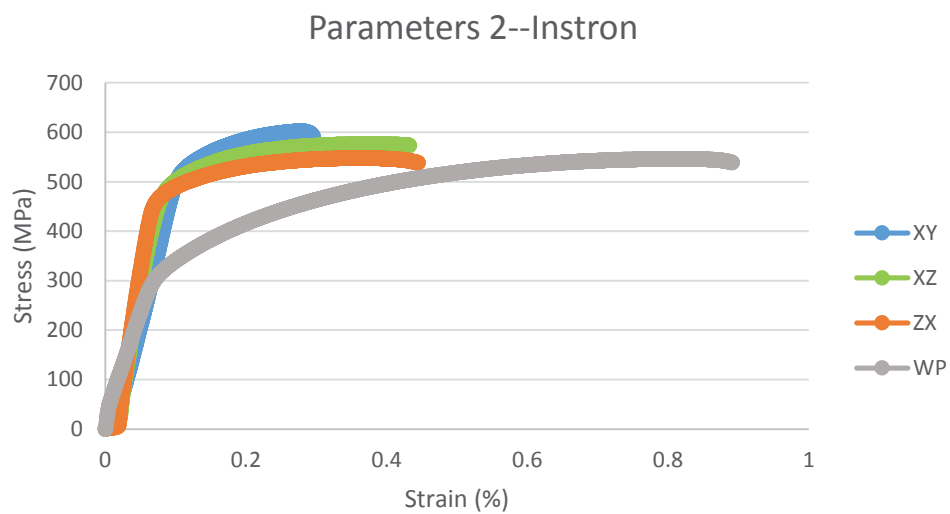


Figure 37: Stress-strain curves of the set of parameters and wrought plate components using the Instron crosshead extension for yield and ductility

The averaged tensile values can be seen in Table 12 and once again compared to the Senvol database.

Table 12: Tensile Properties of Parameter Group 2 and Wrought Plate Samples

<b>Specimen Group</b>	<b>E (GPa)</b>	<b>UTS (MPa)</b>	<b><math>\sigma_y</math> (MPa)</b>	<b>Reduction of Area (%)</b>
<i>XY</i>	226 ± 43	604 ± 15	492 ± 17	31 ± 6
<i>ZX</i>	206 ± 55	560 ± 7	464 ± 12	46 ± 4
<i>XZ</i>	195 ± 14	589 ± 47	427 ± 64	31 ± 6
<i>WP</i>	191 ± 22	585 ± 57	260 ± 59	67 ± 2
<i>Senvol Results [84]</i>	150-195	585-686	-	45-59
<i>Senvol Post-Processed Results [84]</i>	147-194	575-615	-	56-74

As seen from the first process parameter results, the yield strengths of the printed samples are much greater in relation to the wrought samples. However, this second set of process parameters produced parts that either are comparable or surpass the tensile qualities of the wrought steel, except for their ductility. The flat-printed specimens have the best attributes while the on-edge specimens have the worst yield and modulus values. The vertically-built specimens had medial tensile characteristics, but the best ductility characteristic and the closest to wrought steel. This second set of parameter specimens are at the high end or above the reported elasticity values from the Senvol database,

though the UTS values are at the bottom of the range or below the reported values. Just like with the first set of parameter specimens the ductility results are comparable with the database in the *ZX* orientation.

These parts, specifically the second set of parameters, compares unfavorably to best results reported by Tolosa et al. [37], but are fairly comparable to the worst case scenarios. However, like in the first set of parameter specimens and from literature, the tensile results show the anisotropic properties with the *XY* specimens having the best properties, which is in agreement with [15, 36]. Part of this is due to the *XY* specimens being pulling parallel to the build layers, while the *ZX* specimens are pulled perpendicular to the build layers which means the layers are pulled apart. It is surprising that the *XZ* specimens were stronger since they are also pulled parallel to the build layers, however since they are printed on-edge there is not the same melt pool overlap to increase the strength. For all SLM specimens, the increase of the yield strength compared to wrought parts is due to the printing process and the rapid solidification that occurs. The rapid solidification of particles can cause smaller grain sizes, resulting in higher yield values.

SEM images of the fracture surfaces of the second process parameters indicate ductile fracture for the *XY* (Figure 37a) and *ZX* (Figure 37b) orientations, with possible brittle fracture in the *XZ* (Figure 37c) orientation. The micrographs show little to no defects, especially when compared the first set of parameters. The higher strengths and ductility of the second parameter set may be due to the smaller diameter dimples and fewer defects. From the two *ZX* micrographs the comparable dimples to the wrought plate fracture surface could explain the higher ductility values than the other AM orientations.

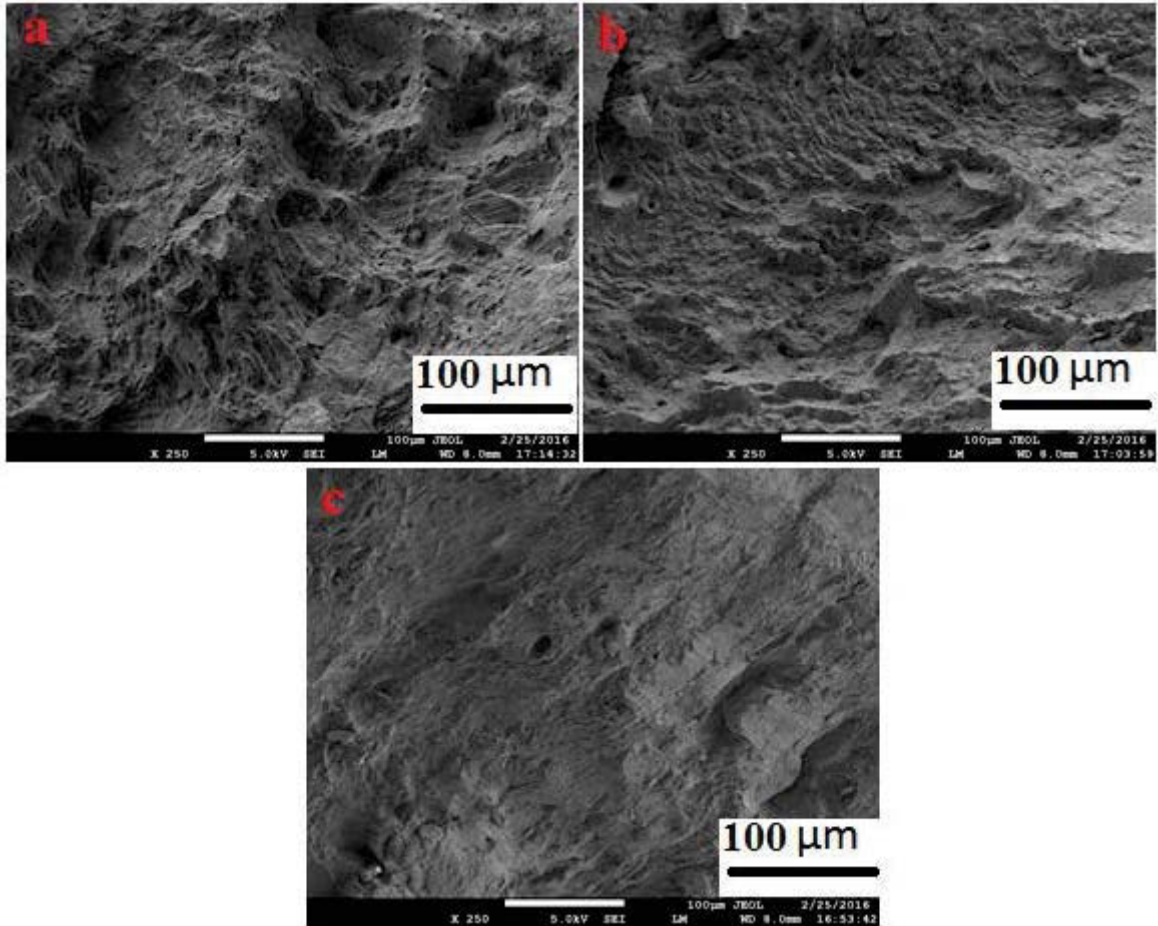


Figure 38: (a) Secondary backscatter images of parameter 2 tensile fracture surface at 250x of the XY orientation, (b) ZX orientation, (c) XZ orientation

These analyses leads to an interesting value for printed material: the ratio of the yield and tensile strengths. Typically the greater this ratio is for metallic alloys, the greater the drop in elongation will be [36]. The ratio of the SLM samples is greater than 0.8 (except for the XZ orientation) while usually keeping elongation values within the accepted range of 316L (40-45%). This is in agreement to the work done by Tolosa et al. [37], where it is noted that the ratio of wrought 316L is typically about 0.4, while their printed samples were typically higher than 0.9 while also maintaining good elongation values (25-44%).

Even though the second set of parameter tensile specimens outperformed the wrought specimens and older studies [15], they did not reach the values reported elsewhere in recent years [36]. While density certainly is one reason for this, another possible cause was discovered in high magnification SEM images of the fracture surfaces of the AM specimens. Some form of embedded contamination was found in each of the specimens, which suggests that it is not contamination from preparation or storage. After noticing the impurities, the areas were examined using the LBE backscatter and EDAX detectors to ascertain what they could be. Images were taken using the LBE backscatter mode at 5,000x and 15 kV, then spot scanned on the matrix material and the contaminant areas with the EDAX detector to determine elemental compositions. The matrix area shows up lighter due to the composition containing heavier elements and is close to the expected composition by weight, with large amounts of Fe (~56%), Cr (~15%), and Ni (~10%) as shown in Figure 38.

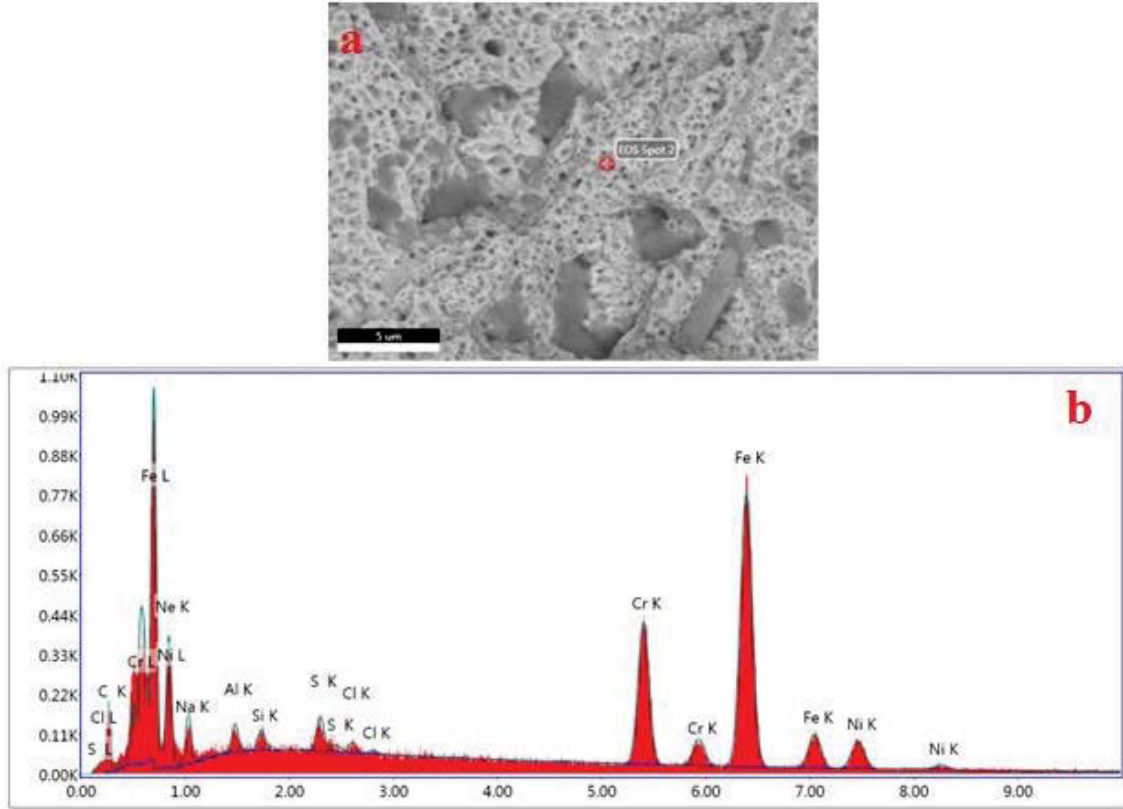


Figure 39: (a) Backscatter electron image of matrix in ZX orientation of parameter 2 tensile fracture surface, (b) EDS spectrum collected from the spot shown in (a).

Another EDS spot scan was done on a darker area, which suggest a lighter elemental composition, and it determined that there was a large jump in Cl composition (from 0.39% to 7.83%). While the Cl peaks were doubted at first, other options (Mo and Nb) were all heavier than the matrix and would have then appeared lighter in the contrast of the image, as seen in Figure 39. Similar results were found in the other tensile samples.



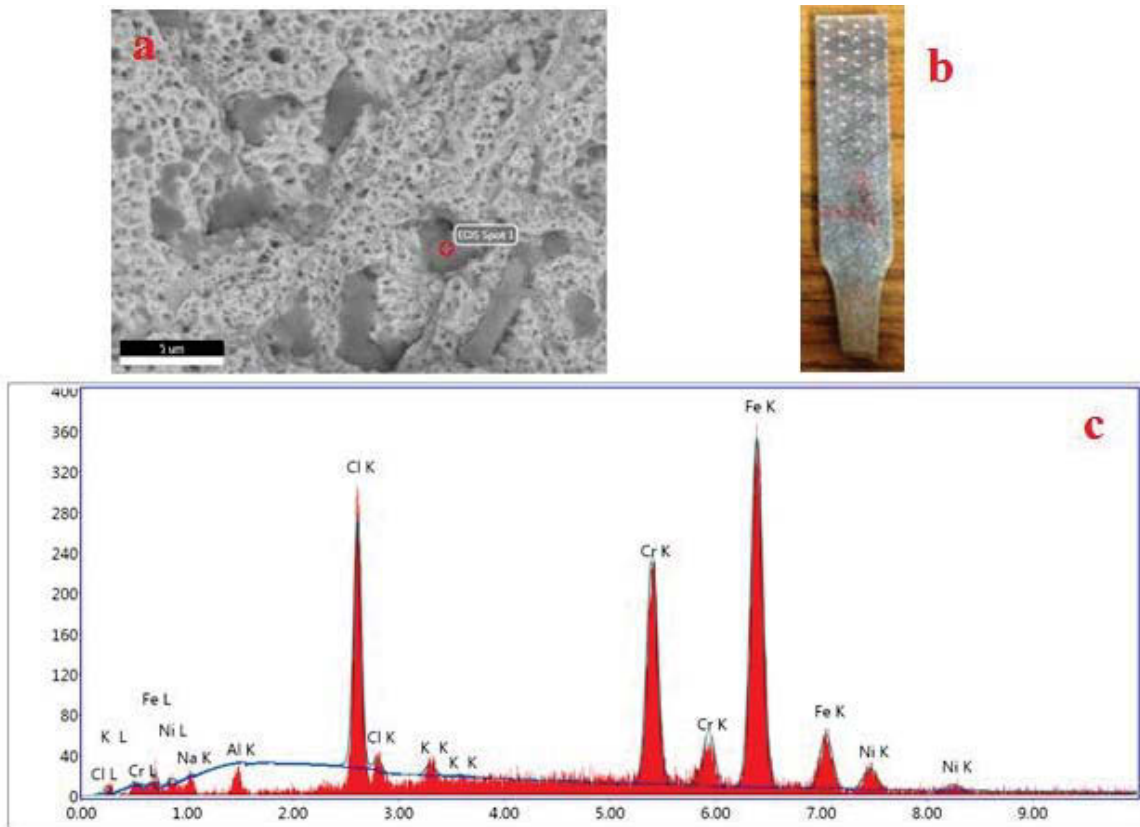


Figure 40: (a) Backscatter electron image of matrix in ZX orientation of parameter 2 tensile fracture surface, (b) image of tensile specimen, (c) EDS spectrum collected from the spot shown in (a).

### 3.3.3 Split-Hopkinson Compression Testing

Dynamic compression tests were done using a REL Split-Hopkinson pressure bar with the striker bar propelled by a gas gun. Using SURE-Pulse software and specimen measurements high-strain rate stress-strain curves were created, as well as other inherent material properties. A typical stress-strain curve as given by the software can be seen in Figure 40. The oscillations shown in the stress-strain curve is due to the momentum trap used to stop the transmission bar.

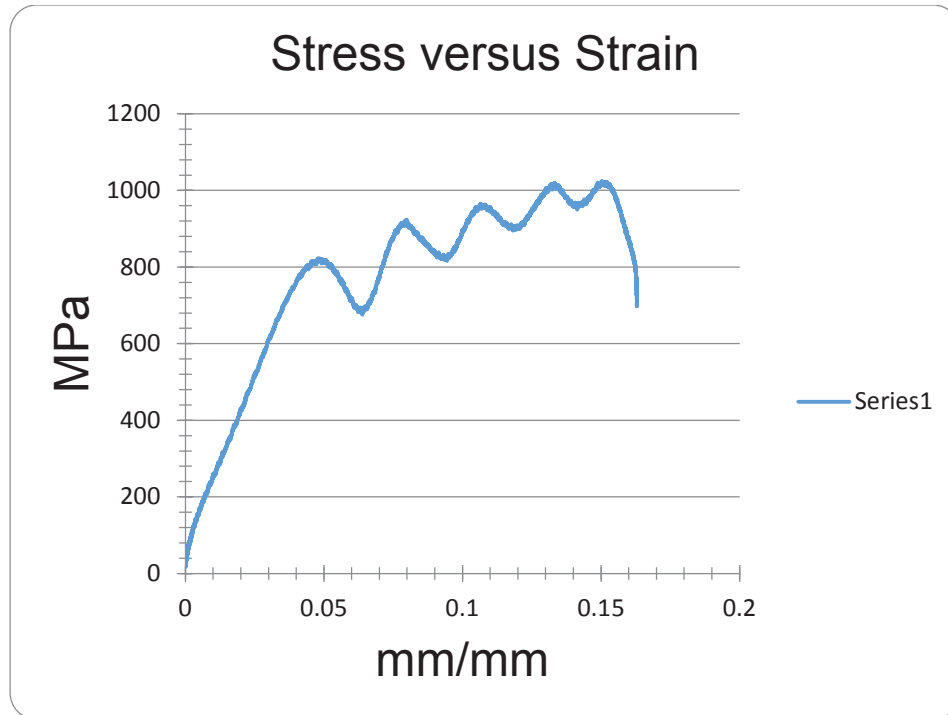


Figure 41: Stress versus strain curve as given by the SURE-Pulse software. This is the stress-strain curve of specimen ZX-3 from the first set of process parameters.

From these plots and the data determined by the software the elastic modulus, max compressive strength, and 0.2% yield strength could be determined and can be seen in Table 13. The average strain rate of the first process parameters and wrought tests is  $2200 \text{ s}^{-1}$ , while the average strain rate of for the second process parameter tests was  $1700 \text{ s}^{-1}$ .

Table 13: Split-Hopkinson compression results with different process parameters and print orientations then compared to wrought specimens.

<b>Specimen Group</b>	<b>E (GPa)</b>	<b>Max Strength (MPa)</b>	<b><math>\sigma_y</math> (MPa)</b>
<i>XY-1</i>	$31 \pm 30$	$1017 \pm 44$	$768 \pm 105$
<i>ZX-1</i>	$33 \pm 16$	$1017 \pm 27$	$776 \pm 49$
<i>ZX-2</i>	$66 \pm 58$	$1063 \pm 161$	$616 \pm 172$
<i>WP</i>	$43 \pm 23$	$1202 \pm 166$	$1020 \pm 118$

This data represents a trend that is seen in the literature of past use of SHPB experiments: that materials are affected by strain rate such that they exhibit greater ultimate and yield strengths at greater strain rates. This is due to the fact that work hardening increases with increasing strain rate. This occurs because of the microstructural transformation of austenite to martensite caused by the plastic deformation of stainless steel that occurs at high strain rates [85]. However, this strain rate sensitivity decreases at differing high strain rates [86]. For SHPB compression testing it is also shown that the results are homogeneous and not adversely affected by print orientation. The elastic modulus from a SHPB experiment is often disregarded due to the inaccuracy of measuring specimen deformation and, for that reason,  $E$  values measured are typically only 30-50% of the values from quasi-static experiments [56]. Table 14 gives SHPB results of a specimen from parameter/orientation each group at a similar average strain rate.

Table 14: SHPB compression results at similar average strain rate values.

<b>Specimen Name</b>	<b>Average Strain Rate (1/s)</b>	<b>Elastic Modulus (GPa)</b>	<b>Ultimate Strength (Mpa)</b>	<b>Yield Strength (MPa)</b>
<i>XY1-1</i>	1924	103.1	1109	531
<i>ZX1-1</i>	2000.3	22.87	957	782
<i>ZX2-9</i>	2037.7	17.07	925	717

The max and yield strengths are close to those reported by Lee and Chiu [57], who tested samples of relative sintered densities of 316L at 83%, 88%, and 93%. At a strain rate of  $3000 \text{ s}^{-1}$  they reported fracture stresses of approximately 1050 MPa, while at a higher strain rate of  $9000 \text{ s}^{-1}$  there was a fracture stress of about 1200 MPa for the 93% density specimen. The yield strengths for the 83%, 88%, and 93% dense specimens at a strain rate of  $3000 \text{ s}^{-1}$  were reported as approximately 375, 395, and 420 MPa, respectively. They concluded that the mechanical response of sintered 316L is sensitive to both strain rate and density at low and high strain rates. Their data shows that the yield strengths were much greater at high (dynamic) strain rates than at quasi-static rates. Furthermore, they concluded that fracture strain decreases with increasing strain rate and relative density.

### 3.3.4 Charpy V-Notch Impact Testing

Charpy V-notch tests were performed on a Tinius Olsen IT 406 mechanism with approximately 300 foot-pounds of energy. The energy absorbed by each specimen before fracturing was recorded and then averaged for each process parameter and orientation group. These results and results from other 316L studies can be seen in Table 15. Tolosa

et al. [37] tested SLM Charpy specimens with the best case scenario being printed 30° to the XY plane and worst case scenario 0° to the ZX plane. Ganesh et al. [43] printed specimens in both the XY and ZX orientations for testing.

Table 15: Charpy V-notch results from both parameter groups

<b>Specimen Group</b>	<b>Energy Absorbed (J)</b>
<i>XY-1</i>	29 ± 9
<i>ZX-1</i>	16 ± 5
<i>XY-2</i>	81 ± 9
<i>ZX-2</i>	128 ± 31
<i>XZ-2</i>	58 ± 13
<i>Tolosa et al. [37] XY SLM 316L</i>	63.3
<i>Tolosa et al. [37] ZX SLM 316L</i>	50.3
<i>Ganesh et al. [43]LRM 316L</i>	90-110

These results compare unfavorably to reported values of traditionally manufactured Charpy V-notch specimens, either  $\geq 75$  J [36] or 105 J [43], except for in the ZX direction in from the second set of parameters. Though the AM produced Charpy specimens do not compare favorably to those traditionally manufactured, those printed using the second parameter set do compare favorably to other reported 316L AM produced samples. Tolosa et al. [37] reported ductile fracture and that porosity was not observed previous to rupture. Ganesh et al. [43] found mixed fracture appearances, with

both dimples and cleavage-like flat facets on the fracture surfaces. Fracture surfaces in this study appear to be almost entirely ductile, which is seen by the dimple-like fracture surfaces seen in Figure 41.

Once again, examinations of the fracture surfaces of the median specimen from each parameter and orientation were done using the FE SEM to determine why the specimens performed so poorly. These images illustrate the presence of loose powder that is not fully melted, or not melted at all, throughout most of the specimens. This is most likely due to the laser energy density being too low for an acceptable build, though it should be noted that for the thinner tensile specimens this defect is not apparent. Not having fully melted particles weakens specimens and are crack initiation locations. These facts are especially obvious in the first parameter specimens, as seen in Figure 41a in the highlighted area. The second parameter specimens appear denser and fully melted, as seen in Figure 41b, but still there is crack initiation from defects seen in the highlighted area.

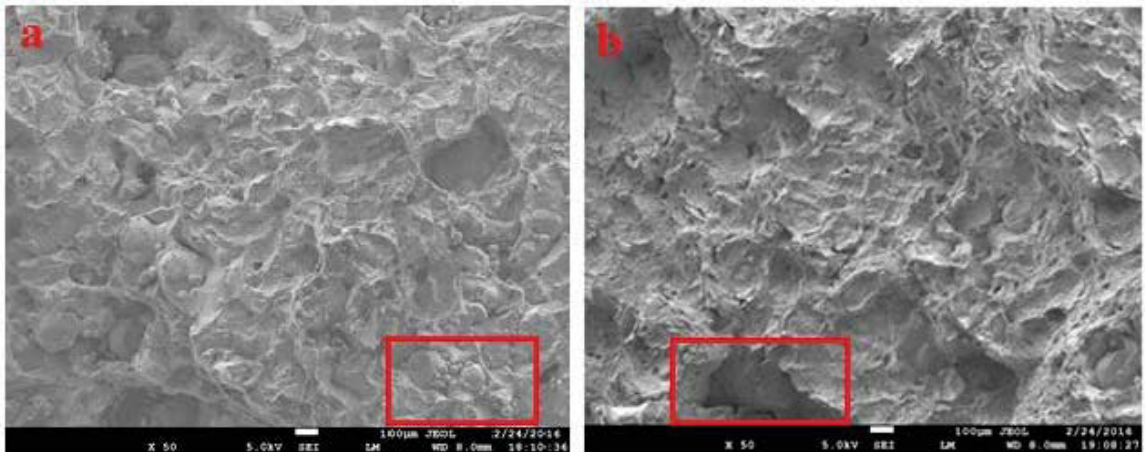


Figure 42: (a) Secondary backscatter images taken at 50x on Charpy fracture surfaces: loose particulates from lack of fusion and defect cracks in the first parameter set ZX orientation and (b) a more acceptable fracture surface from the second parameter set ZX orientation

Even if just the different orientations of the second set of parameters are investigated, the fracture surfaces illustrate the vast differences in impact toughness between them. The two orientations, *XY* and *ZX*, with the highest impact toughness, and are within comparison to wrought 316L, appear to be fully melted and without obvious defects to propagate cracks. In the *XZ* orientation, however, there are localized regions of loose powder and multiple large pores which severely weakens the impact resistance of the specimen. These surfaces are shown below in Figure 42. Even so, the *XY* specimens were not as tough as the *ZX* and it is believed that lack of fusion defects initiating and propagating cracks is the cause for this. An example is seen in Figure 43, where a large void creates a crack front across the image.

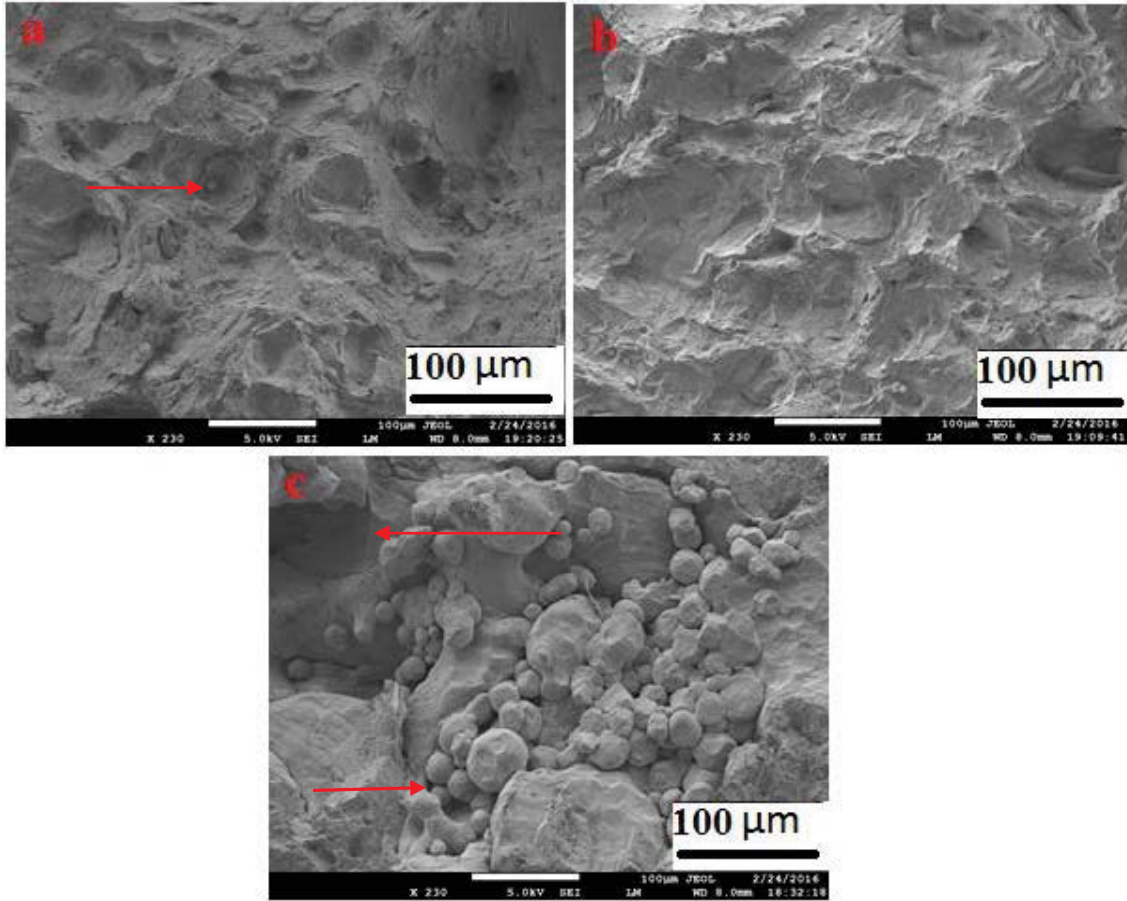


Figure 43: (a) Secondary backscatter images at 230x of second parameter Charpy fracture surfaces of XY, (b) ZX, and (c) XZ.

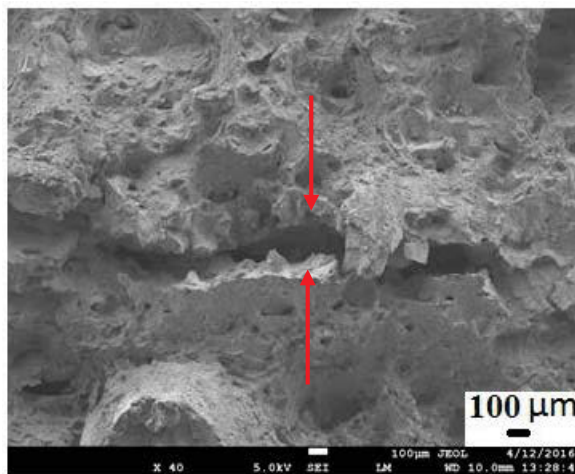


Figure 44: Crack propagation and defects in Charpy fracture surface from parameter set 2 in the XY orientation



It is not surprising that in the first set of parameters that the *XY* specimens had a higher impact toughness considering that they had the notch machined and force impacted perpendicular to the build layers. The *ZX* specimens, on the other hand, had the notch machined and were impacted parallel to the build layers, eliminating the extra resistance that the *XY* specimens enjoyed. Therefore, it is somewhat surprising that in the second set of parameters that the *ZX* specimens had the highest impact toughness of the set. It is concluded that the thinner build volume per layer allowed the *ZX* specimens to experience a more complete melting profile and, consequently, a higher density finished part. With a larger build volume per layer, the *XY* and *XZ* specimens did not appear to be fully melted and had a higher percentage of lack of fusion or porosity defects that hindered their impact toughness values. Even though the notches were machined on different planes, they were still perpendicular to the build layer, which should yield higher impact resistances.

## Chapter 4: Conclusions and Future Work

The purpose of this work was to determine whether selectively laser melted stainless steel 316L parts could be used in high-strain rate applications with the process parameters originally on the machine and optimum parameters supplied by Renishaw. The parts were printed on a Renishaw AM250 with two different parameter sets and mechanically tested in the quasi-static and dynamic strain ranges to qualify the worthiness of the parts for industry, particularly for aerospace, medicine, and defense applications. Tests included Brinell and Rockwell D hardness, quasi-static tensile, Split-Hopkinson compression, and Charpy V-notch impact in order to get as varied an understanding of the material as possible. The microstructures, defects, and fracture surfaces were explored using both optical and scanning electron microscopes to quantify possible reasons for the mechanical behaviors of the different parts. The results were then compared to wrought 316L and to results reported in literature.

When relating the AM results of this study to the wrought results and to those from literature, it was determined that overall the original processing parameters produce unfavorable material properties due to defects. On the other hand, the second processing parameters result in material properties comparable to both the wrought values and the literature values, especially in the *XY* and *ZX* orientations. The first parameter parts suffered from a large amount of porosity and a lack of fusion defects (un-melted particles). However, due to the nature of the SLM process and the ensuing grain sizes formed by rapid solidification of molten metal, the resulting parts have higher yield strengths, even with lower ductility values. The second set of parameters increased the mechanical properties almost across the board, and created parts denser and with fewer

defects. Still, even with an increased laser energy density, the fracture surfaces of the Charpy V-notch specimens showed particles not fully melted. In every test except the Split-Hopkinson, the results proved that the SLM parts are affected by both density and print orientation, either due to build layers or particle melting.

Even as the mechanical properties differed greatly from the wrought specimens, the microstructures examined also diverged from what is typically seen in traditionally manufactured 316L. While 316L is usually considered an austenitic steel, other structures hypothesized to be martensite were found in the etched micrographs; this may also help explain the increased yields and decreased ductility. The SEM images exposed lack of fusion defects as well as the increased density from parameter set 1 to set 2. However, when examining the specimens the grain structure was not fully visible; in the future, further examinations of the polished samples using Vilella's reagent will hopefully yield better microstructures. A better determination of the porosity levels of the printed specimens is also needed to get a better understanding of the properties and microstructure of the parts.

Overall, the second set of parameter parts, particularly in the ZX orientation, appear to be close to wrought properties. The results are more promising in the dynamic strain range, but further optimization of the process parameters is recommended for future work. An increase in energy density for parts thicker than tensile bars could increase the density and mechanical properties, while reducing defects that plague SLM parts. It is also recommended that high temperature tensile testing be performed in order to determine the material's Johnson-Cook parameters. Quasi-static compression testing would be helpful to better understand the strain-rate sensitivity of 316L when compared

to the SHPB results, though a more varied high strain-rate profile is also suggested. Other areas that can be investigated include potential benefits of post-processing techniques such as HIP to increase density or Alcoa's Ampliforge process. In the Ampliforge process, a part is 3D printed to a nearly finished state and is then treated with a traditional manufacturing process like forging to enhance its mechanical properties [87].

This research was done with the hope of reaching a better understanding of the response of SLM manufactured stainless steel 316L to quasi-static and dynamic strain rates, while exploring multiple process parameters and print orientations. These preliminary findings from exploring the high-strain rate responses should ideally lead to further research in this area. While there are currently some industrial applications that can utilize the SLM process, with further optimization and research the breadth of applications can be expanded to those requiring high density and high strengths all while saving time and material in comparison to traditionally manufactured parts.

## References

1. Gu, D., 2015, *Laser Additive Manufacturing of High-Performance Materials*, Springer Science & Business Media, Berlin.
2. Gibson, I., Rosen, D. and Stucker, B., 2015, *Advanced Manufacturing Technologies*, 2<sup>nd</sup> Ed., Springer Science & Business Media, New York, NY.
3. Utela, B., Storti, D., Anderson, R., and Ganter, M., 2008, "A review of process development steps for new material systems in three dimensional printing (3DP)," *Journal of Manufacturing Processes*, 10, pp. 96-104.
4. ASTM, 2012, "Standard Terminology for Additive Manufacturing Technologies," F2792-12a.
5. Kumar, S. and Pityana, S., 2011, "Laser-based additive manufacturing of metals," *Advanced Materials Research*, 227, pp. 92-95.
6. Zhou, X., Li, K., Zhang, D., Liu, X., Ma, J., Liu, W., and Shen, Z., 2015, "Textures formed in a CoCrMo alloy by selective laser melting," *Journal of Alloys and Compounds*, 631, pp. 153-164.
7. Stwora, A. and Skrabalak, G., 2013, "Influence of selected parameters of Selective Laser Sintering process on properties of sintered materials," *Journal of Achievements in Materials and Manufacturing Engineering*, 61(2), pp. 375-380.
8. Gong, H., Gu, H., Zeng, K., Dilip, J.J.S., Pal, D., Stucker, B., Christiansen, D., Beuth, J., and Lewandowski, J.J., 2014, "Melt Pool Characterization for Selective Laser Melting of Ti-6Al-4V Pre-alloyed Powder," In *Solid freeform fabrication symposium*.

9. Yadroitsev, I. and Smurov, I., 2011, "Surface Morphology in Selective Laser Melting of Metal Powders," *Physics Procedia*, 12, pp. 264-270.
10. Cherry, J.A., Davies, H.M., Mehmood, S., Lavery, N.P., Brown, S.G.R., and Sienz, J., 2014, "Investigation into the effect of process parameters on microstructural and physical properties of 316L stainless steel parts by selective laser melting," *The International Journal of Advanced Manufacturing Technology*, 76(5-8), pp.869-879.
11. Spierings, A.B. and Levy, G., 2009, "Comparison of density of stainless steel 316L parts produced with selective laser melting using different powder grades," In *Proceedings of the Annual International Solid Freeform Fabrication Symposium*, pp. 342-353, Austin, TX.
12. Trelewicz, J.R., Halada, G.P., Donaldson, O.K., and Manogharan, G., 2016, "Microstructure and Corrosion Resistance of Laser Additively Manufactured 316L Stainless Steel," *JOM*, 68(3), pp. 850-859.
13. Simonelli, M., Tse, Y.Y., and Tuck, C., 2014, "Effect of the build orientation on the mechanical properties and fracture modes of SLM Ti-6Al-4V," *Materials Science and Engineering: A*, 616, pp. 1-11.
14. Tsopanos, S., Mines, R.A.W., McKown, S., Shen, Y., Cantwell, W.J., Brooks, W., and Sutcliffe, C.J., 2010, "The Influence of Processing Parameters on the Mechanical Properties of Selectively Laser Melted Stainless Steel Microlattice Structures," *Journal of Manufacturing Science and Engineering*, 132(4), pp. 041011.
15. Yadroitsev, I. and Smurov, I., 2010, "Selective laser melting technology: from the single laser melted track stability to 3D parts of complex shape," *Physics Procedia*, 5, pp. 551-560.

16. Khan, M. and Dickens, P., 2010, "Selective Laser Melting (SLM) of pure gold," *Gold Bulletin*, 43(2), pp. 114-121.
17. Santos, E., Abe, F., Kitamura, Y., Osakada, K., and Shiomi, M., 2002, "Mechanical Properties of Pure Titanium Models Processed by Selective Laser Melting," In *Proceedings of the Solid Freeform Fabrication Symposium*, pp. 180-186.
18. Simonelli, M., Tse, Y.Y., and Tuck, C., 2014, "On the Texture Formation of Selective Laser Melted Ti-6Al-4V," *Metallurgical and Materials Transactions A*, 45(6), pp. 2863-2872.
19. Qui, C., Adkins, N.J.E., and Attallah, M.M., 2013, "Microstructure and tensile properties of selectively laser-melted and of HIPed laser-melted Ti-6Al-4V," *Materials Science and Engineering: A*, 578, pp. 230-239.
20. Qui, C., Panwisawas, C., Ward, M., Basoalto, H.C., Brooks, J.W., and Attallah, M.M., 2015, "On the role of melt flow into the surface structure and porosity development during selective laser melting," *Acta Materialia*, 96, pp. 72-79.
21. Vrancken, B., Thijs, L., Kruth, J.P., and Van Humbeeck, J., 2014, "Microstructure and mechanical properties of a novel  $\beta$  titanium metallic composite by selective laser melting," *Acta Materialia*, 68, pp. 150-158.
22. Vrancken, B., Cain, V., Knutsen, R., and Van Humbeeck, J., 2014, "Residual stress via the contour method in compact tension specimens produced via selective laser melting," *Scripta Materialia*, 87, pp. 29-32.
23. Yadroitsev, I., Thivillon, L., Bertrand, Ph., and Smurov, I., 2007, "Strategy of manufacturing components with designed internal structure by selective laser melting of metallic powder," *Applied Surface Science*, 254, pp. 980-983.

24. Badrossamay, M. and Childs, T.H.C., 2007, "Further studies in selective laser melting of stainless and tool steel powders," *International Journal of Machine Tools & Manufacture*, 47(5), pp. 779-784.
25. Simchi, A., 2006, "Direct laser sintering of metal powders: Mechanism, kinetics and microstructural features," *Materials Science and Engineering: A*, 428(1), pp. 148-158.
26. Rombouts, M., Kruth, J.P., Froyen, L., and Mercelis, P., 2006, "Fundamentals of Selective Laser Melting of alloyed steel powders," *CIRP Annals-Manufacturing Technology*, 55(1), pp. 187-192.
27. Kruth, J.P., Froyen, L., Van Vaerenbergh, J., Mercelis, P., Rombouts, M., and Lauwers, B., 2004, "Selective laser melting of iron-based powder," *Journal of Materials Processing Technology*, 149(1), pp. 616-622.
28. Ma, M., Wang, Z., Gao, M., and Zeng, X., 2015, "Layer thickness dependence of performance in high-power selective laser melting of 1Cr18Ni9Ti stainless steel," *Journal of Materials Processing Technology*, 215, pp. 142-150.
29. Simchi, A. and Pohl, H., 2003, "Effects of laser sintering processing parameters on the microstructure and densification of iron powder," *Materials and Engineering: A*, 359(1), pp. 119-128.
30. Simchi, A., Petzoldt, F., and Pohl, H., 2003, "On the development of direct metal laser sintering for rapid tooling," *Journal of Materials Processing Technology*, 141(3), pp. 319-328.
31. Yasa, E., Kempen, K., Kruth, J.P., Thijs, L., and Van Humbeeck, J., 2010, "Microstructure and mechanical properties of maraging steel 300 after selective laser melting," In *Solid Freeform Fabrication Symposium Proceedings*, pp. 383-396.



32. Yadroitsev, I., Bertrand, Ph., and Smurov, I., 2007, "Parametric analysis of the selective laser melting process," *Applied Surface Science*, 253(19), pp. 8064-8069.
33. Brown, B., 2014, "Characterization of 304L stainless steel by means of minimum input energy on the selective laser melting platform," Master's thesis, Paper 7322, Missouri University of Science and Technology, Rolla, MO.
34. Yasa, E. and Kruth, J.P., 2011, "Microstructural investigation of Selective Laser Melting 316L stainless steel parts exposed to laser re-melting," *Procedia Engineering*, 19, pp. 389-395.
35. Li, R., Shi, Z., Wang, L., Liu, J., and Jiang, W., 2010, "Densification behavior of gas and water atomized 316L stainless steel powder during selective laser melting," *Applied Surface Science*, 256(13), pp. 4350-4356.
36. Majumdar, J.D., Pinkerton, A., Liu, Z., Manna, I., and Li, L., 2005, "Microstructure characterisation and process optimization of laser assisted rapid fabrication of 316L stainless steel," *Applied Surface Science*, 247(1), pp. 320-327.
37. Tolosa, I., Garcíandia, F., Zubiri, F., Zapirain, F., and Esnaola, A., 2010, "Study of mechanical properties of AISI 316 stainless steel processed by 'selective laser melting', following different manufacturing strategies," *The International Journal of Manufacturing Technology*, 51(5-8), pp. 639-647.
38. Riemer, A., Leuders, S., Thöne, M., Richard, H.A., Tröster, T., and Niendorf, T., 2014, "On the fatigue crack growth behavior in 316L stainless steel manufactured by selective laser melting," *Engineering Fracture Mechanics*, 120, pp. 15-25.
39. Mindt, H.W., Megahed, M., Lavery, N.P., Giordimaina, A. and Brown, S.G.R., 2016, "Verification of Numerically Calculated Cooling Rates of Powder Bed Additive

- Manufacturing,” In *TMS 2016: 145 Annual Meeting & Exhibition: Supplemental Proceedings*, pp. 205-212, John Wiley & Sons, Inc.
40. Gray III, G.T., Lienert, T.J., Carpenter, J.S., Trujillo, C.P., Livescu, V., Sutton, J.O., Chen, S.R., Fensin, S., Martinez, D., Forsyth, R.T., Morrow, B., Coughlin, D.R., Hudson, R.W., Thoma, D.J., and Teter, D.F., 2014, “Quasi-static and Dynamic Performance of 316L Stainless Steel Fabricated through Directed Energy Additive Manufacturing,” PowerPoint slides, Los Alamos Nation Security, LLC.
41. Blandford, R.K., Morton, D.K., Snow, S.D., and Rahl, T.E., 2007, “Tensile Stress-Strain Results for 304L and 316L Stainless Steel Plate at Temperature,” In *ASME 2007 Pressure Vessels and Piping Conference*, pp. 617-628, American Society of Mechanical Engineers.
42. Keicher, D.M., Romero, J.A., Atwood, C.L., Griffith, M.L., Jeantette, F.P., Harwell, L.D., Greene, D.L. and Smugeresky, J.E., 1996, “Free form fabrication using the laser engineered net shaping (LENS™) process,” (No. SAND--96-2690C; CONF-9606165--3), Sandia National Labs, Albuquerque, NM.
43. Ganesh, P., Kaul, R., Sasikala, G., Kumar, H., Venugopal, S., Tiwari, P., Rai, S., Prasad, R.C., and Kukreja, L.M., 2014, “Fatigue Crack Propagation and Fracture Toughness of Laser Rapid Manufactured Structures of AISI 316L Stainless Steel,” *Metallography, Microstructure, and Analysis*, 3(1), pp. 36-45.
44. Król, M., Dobrzański, L.A., Reimann, Ł., and Czaja, I., 2013, “Surface quality in selective laser melting of metal powders,” *Archives of Materials Science and Engineering*, 60(2), pp. 87-92.

45. Paul, C.P., Ganesh, P. Mishra, S.K., Bhargava, P., Negi, J., and Nath, A.K., 2007, "Investigating laser rapid manufacturing for Inconel-625 components," *Optics & Laser Technology*, 39(4), pp. 800-805.
46. Leuders, S., Thöne, M., Riemer, A., Niendorf, T., Tröster, T., Richard, H.A., and Maier, H.J., 2013, "On the mechanical behavior of titanium alloy TiAl6V4 manufactured by selective laser melting: Fatigue resistance and crack growth performance," *International Journal of Fatigue*, 48, pp. 300-307.
47. Cahn, R.W., Haasen, P., and Kramer, E.J. (Eds.), 1991, *Materials Science and Technology: A Comprehensive Treatment* (Volume 15: Processing of Metals and Alloys), VCH Publishers Inc., New York, NY.
48. Hofmeister, W., Griffith, M., Ensz, M., and Smugeresky, J., 2001, "Solidification in direct metal deposition by LENS processing," *Journal of Materials*, 53, pp. 30-34.
49. Kruth, J.P., Badrossamay, M., Yasa, E., Deckers, J., Thijs, L., and Humbeeck, J.V., 2010, "Part and material properties in selective laser melting of metals," In *Proceedings of the 16<sup>th</sup> international symposium on electromachining*.
50. Kalpakjian, S., 1995, *Manufacturing Engineering and Technology*, 3<sup>rd</sup> Ed., Addison-Wesley, Reading, MA.
51. ASTM, 2009, "Standard Test Methods for Tension Testing of Metallic Materials," E8/8M-09.
52. Callister Jr., W.D., 2003, *Materials Science and Engineering: An Introduction*, John Wiley & Sons, Inc., New York, NY.

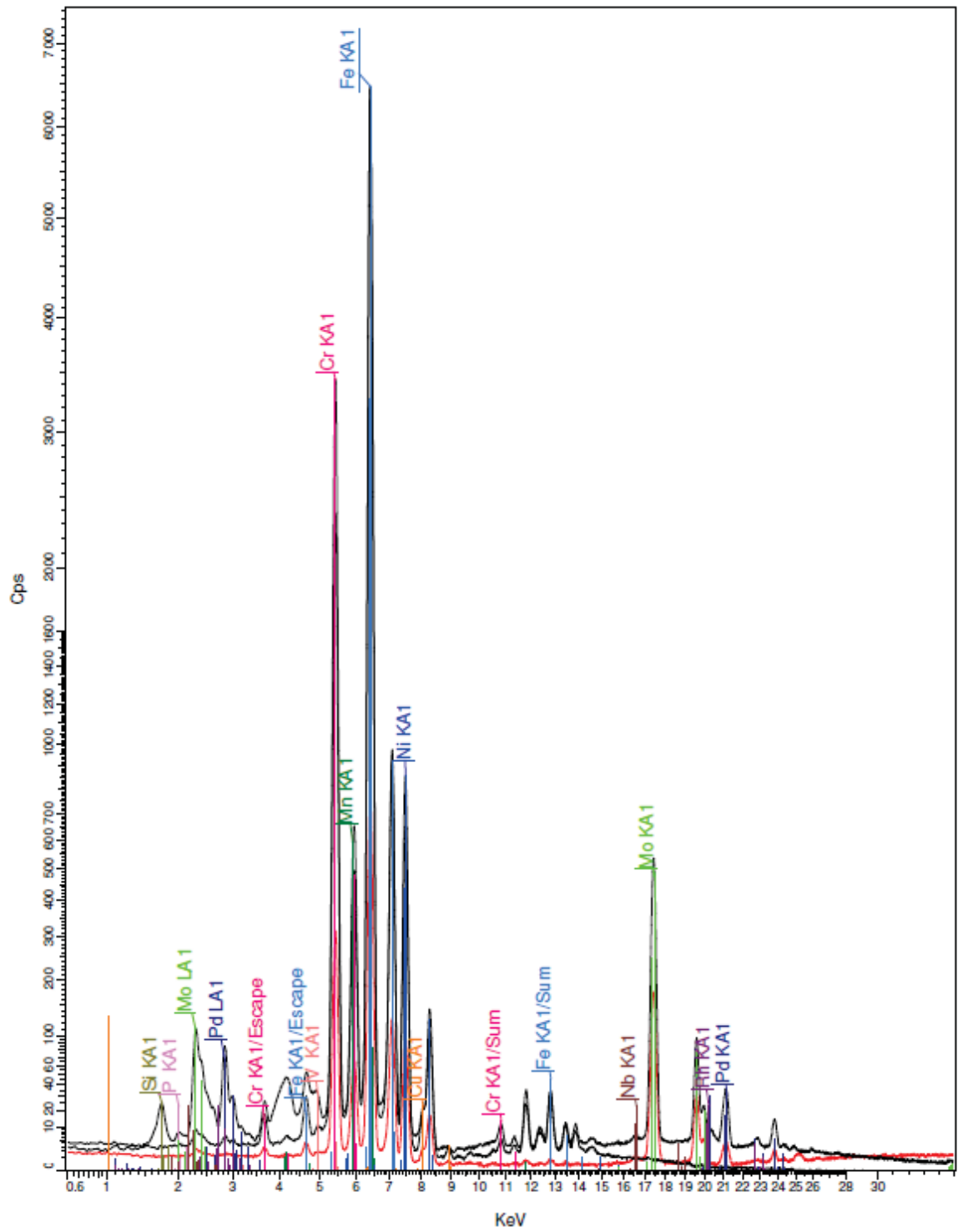
53. Kahlen, F.J. and Kar, A., 2001, "Tensile Strengths for Laser-Fabricated Parts and Similarity Parameters for Rapid Manufacturing," *Journal of Manufacturing Science and Engineering*, 123(1), pp. 38-44.
54. Ganesh, P., Kaul, R., Paul, C.P., Tiwari, P., Rai, S.K., Prasad, R.C., and Kukreja, L.M., 2010, "Fatigue and fracture toughness characteristics of laser rapid manufactured Inconel 625 structures," *Materials Science and Engineering: A*, 527(29), pp. 7490-7497.
55. Chen, W.W. and Song, B., 2010, *Split Hopkinson (Kolsky) Bar: Design, Testing and Applications*, Springer Science & Business Media, Berlin.
56. Kolsky, H., "An Investigation of the Mechanical Properties of Materials at very High Rates of Loading," *Proceedings of the Physical Society, Section B*, 62(11), pp. 676-700.
57. Lee, W.S. and Chiu, C.C., 2006, "Deformation and Fracture Behavior of 316L Sintered Stainless Steel under Various Strain Rate and Relative Sintered Density Conditions," *Metallurgical and Materials Transactions A*, 37(12), pp. 3685-3696.
58. Winter, R.E., Cotton, M., Harris, E.J., Maw, J.R., Chapman, D.J., Eakins, D.E., and McShane, G., 2014, "Plate-impact loading of cellular structures formed by selective laser melting," *Modelling and Simulation in Materials Science and Engineering*, 22(2), pp. 025021.
59. Lee, W.S., Lin, C.F., and Liu, T.J., 2006, "Strain rate dependence of impact properties of sintered 316L stainless steel," *Journal of Nuclear Materials*, 359(3), pp. 247-257.

60. Lee, W.S., Lin, C.F., Chen, T.H., and Luo, W.Z., 2012, "High temperature deformation and fracture behavior of 316L stainless steel under high strain rate loading," *Journal of Nuclear Materials*, 420(1), pp. 226-234.
61. ASTM, 2014, "Standard Test Methods and Definitions for Mechanical Testing of Steel Products," A370-14.
62. ASTM, 2015, "Standard Test Method for Measurement of Fatigue Crack Growth Rates," E647-15.
63. ASTM, 2013, "Standard Test Method for Measurement of Fracture Toughness," E1820-13.
64. Sun, C.T., 2006, *Mechanics of Aircraft Structures*, 2<sup>nd</sup> Ed., John Wiley & Sons, Inc., Hoboken, NJ.
65. Askeland, D.R., Fulay, P.P., and Wright, W.J., 2011, *The Science and Engineering of Materials*, 6<sup>th</sup> Ed., Cengage Learning, Stamford, CT.
66. Kundu, T., 2008, *Fundamentals of Fracture Mechanics*, CRC Press, Boca Raton, FL.
67. Atlas Steels Technical Department, 2013, "Stainless Steel Grade Database," Atlas Steels, Australia.
68. Renishaw, 2012, "Safety Data Sheet: Stainless Steel 316-L SLM Powder," Rev. 1, Renishaw PLC, Staffordshire, UK.
69. Cilas, "Particle Size Analyzers," <http://www.es-france.com/pdf/Cilas-1190.pdf>.
70. Murr, L.E., Gaytan, S.M., Ramirez, D.A., Martinez, E., Hernandez, J., Amato, K.N., Shindo, P.W., Medina, F.R., and Wicker, R.B., 2012, "Metal Fabrication by Additive Manufacturing Using Laser and Electron Beam Melting Technologies," *Journal of Materials Science and Technology*, 28(1), pp. 1-14.

71. Aliakbari, M., 2012, "Additive Manufacturing: State-of-the-Art. Capabilities, and Sample Applications with Cost Analysis," Master's thesis, Royal Institute of Technology, Stockholm, Sweden.
72. Renishaw, 2013, "The Power of Additive Manufacturing," Renishaw PLC, Staffordshire, UK.
73. Stony Brook University, 2016, "Porosity Analysis Procedure," Retrieved from [https://stonybrook.digication.com/esm\\_499\\_research\\_at\\_ctsr/Porosity\\_Analysis](https://stonybrook.digication.com/esm_499_research_at_ctsr/Porosity_Analysis), 11 April 2016.
74. Bramfitt, B.L. and Benschoter, A.O., 2002, *Metallographer's Guide: Practices and Procedures for Irons and Steels*, ASM International, Ann Arbor, MI.
75. ASTM, 2015, "Standard Test Methods for Rockwell Hardness of Metallic Materials," E18-15.
76. ASTM, 2015, "Standard Test Methods for Brinell Hardness of Metallic Materials," E10-15a.
77. Leser, C., "Tensile Properties & the Tension Test," MTS Material Solutions, Eden Prairie, MN.
78. Retrieved from [http://www.engineeringarchives.com/img/les\\_mom\\_tensiletest\\_1.png](http://www.engineeringarchives.com/img/les_mom_tensiletest_1.png).
79. REL, 2014, "SHPB Calibration Manual and Sample Test (Compression)."
80. ASTM, 2012, "Standard Test Methods for Notched Bar Impact Testing of Metallic Materials," E23-12c.
81. Retrieved from <http://atrona.com/charpy-testing.html>.

82. ASTM, 2015, "Standard Specification for Chromium and Chromium-Nickel Stainless Steel Plate, Sheet, and Strip for Pressure Vessels and for General Applications," A240/A240M-15b.
83. *ASM Handbook, Volume 1: Properties and Selection: Irons, Steels, and High-Performance Alloys*, 2005.
84. Senvol Database, 2016, "Materials Results," Retrieved from [http://senvol.com/5\\_material-results/](http://senvol.com/5_material-results/), 2 May 2016.
85. Chalivendra, V., Song, B., and Casem, D., 2012, *Dynamic Behavior of Materials, Volume 1: Proceedings of the 2012 Annual Conference on Experimental and Applied Mechanics*, Chapter 13, Springer, New York.
86. Laubscher, R.F., 1997, "An Evaluation of Strain Rate Sensitivity of Certain Stainless Steels," Ph.D. thesis, Rand Afrikaans University, Johannesburg, South Africa.
87. Alcoa, 3 September 2015, "Alcoa Expands R&D Center to Deepen Additive Manufacturing Capabilities," Retrieved from <http://www.alcoa.com/global/en/news>, 4 May 2016.

# Appendix





TKSS316LPowder (Coupled TwoTheta/Theta)

